Stem Cell Reports
Article
ISSCR
OPEN ACCESS

Gli1$^+$ Cells Couple with Type H Vessels and Are Required for Type H Vessel Formation

Ji Chen,[1,3,4] Meng Li,[1,4] An-Qi Liu,[1,4] Chen-Xi Zheng,[1] Li-Hui Bao,[1,2] Kai Chen,[1,2] Xiao-Lin Xu,[1,2] Jiang-Tao Guan,[1,2] Meng Bai,[1,2] Tao Zhou,[1,2] Bing-Dong Sui,[1] De-Hua Li,[3,*] Yan Jin,[1,*] and Cheng-Hu Hu[1,2,*]

[1]State Key Laboratory of Military Stomatology& National Clinical Research Center for Oral Diseases & Shaanxi International Joint Research Center for Oral Diseases, Center for Tissue Engineering, School of Stomatology, The Fourth Military Medical University, 145 West Changle Road, Xi'an, Shaanxi 710032, China

[2]Xi'an Institute of Tissue Engineering and Regenerative Medicine, Xi'an, Shaanxi 710032, China

[3]Department of Oral Implantology, School of Stomatology, Fourth Military Medical University, Xi'an, Shannxi 710032, China

[4]Co-first author

*Correspondence: lidehua0717@163.com (D.-H.L.), yanjinfmmu@vip.sina.com (Y.J.), chenghu@xiterm.com (C.-H.H.)

https://doi.org/10.1016/j.stemcr.2020.06.007

SUMMARY

Mesenchymal stem/stromal cells (MSCs) reside in the perivascular niche and modulate tissue/organ homeostasis; however, little is known about whether and how their localization and function are linked. Particularly, whether specific MSC subsets couple with and regulate specialized vessel subtypes is unclear. Here, we show that Gli1$^+$ cells, which are a subpopulation of MSCs couple with and regulate a specialized form of vasculature. The specific capillaries, i.e., CD31^{hi}EMCN^{hi} type H vessels, are the preferable vascular subtype which Gli1$^+$ cells are adjacent to in bone. Gli1$^+$ cells are further identified to be phenotypically coupled with type H endothelium during bone growth and defect healing. Importantly, Gli1$^+$ cell ablation inhibits type H vessel formation associated with suppressed bone generation and regeneration. Mechanistically, Gli1$^+$ cells initiate angiogenesis through Gli and HIF-1α signaling. These findings suggest a morphological and functional framework of Gli1$^+$ cells modulating coupled type H vasculature for tissue homeostasis and regenerative repair.

INTRODUCTION

Mesenchymal stem/stromal cells (MSCs) have putative roles of safeguarding adult tissue/organ homeostasis and maintaining regenerative tissue repair, the *in vivo* characteristics of which regarding their specific identity, specialized niches, and the associated function are hot topics in this field (Kfoury and Scadden, 2015; Lemos and Duffield, 2018). Particularly, over the years, the notion that postnatal MSCs reside adjacent to the vasculature has attracted much research interest (Crisan et al., 2008; Guimaraes-Camboa et al., 2017; Shi and Gronthos, 2003). In 2014, researchers demonstrated that glioma-associated oncogene homolog 1 (Gli1) marks perivascular MSC-like cells in the mouse incisor, which express typical MSC surface markers and possess multiple differentiation potentials in culture (Zhao et al., 2014). During the past several years, accumulating evidence suggests that Gli1$^+$ cells are present in various organs where they are embedded in adventitial matrix or make close contact to microvascular endothelial cells (ECs), and possess important biological functions. In this regard, Gli1$^+$ cells represent a subpopulation of MSCs across many organs that are characterized by perivascular location (Kramann et al., 2015, 2016; Schneider et al., 2017; Shi et al., 2017). Notably, MSCs have been documented to stimulate angiogenesis *in vitro* and in cytotherapy or tissue engineering applications (Kasper et al., 2007; Manieri et al., 2015; Piard et al., 2019). However, whether and how the perivascular localization of specific MSCs, in particular Gli1$^+$ cells, affects angiogenesis *in situ* remains unclear.

Recent studies have established a specific capillary subtype in bone, namely type H vessels, which are featured by CD31^{hi}Endomucin (EMCN)^{hi} markers with an interconnected straight column pattern and high proliferative capacity (Kusumbe et al., 2014; Ramasamy et al., 2014). On the other hand, the terminology type L vessels were proposed for the CD31^{lo}EMCN^{lo} sinusoidal vessels. Notably, type H vessels are upstream of type L vessels, and mediate developmental and regenerative angiogenesis in bone (Kusumbe et al., 2014; Ramasamy et al., 2014). Moreover, compared with type L vessels, type H vessels exclusively connect to arteries and possess functional properties to maintain perivascular osteoprogenitors and couple angiogenesis to osteogenesis (Kusumbe et al., 2014). Importantly, the type H endothelium has been revealed as a crucial mediator of bone regeneration and a pharmacological target to counteract bone loss and enhance fracture healing (Kusumbe et al., 2014; Xu et al., 2018). Mechanistically, a series of cellular and molecular basis has been reported to regulate type H vessel formation (Caire et al., 2019; Huang et al., 2016; Ramasamy et al., 2014; Xie et al., 2014; Xu et al., 2018; Yang et al., 2017). Nevertheless, the MSC-mediated regulation of type H vessels is not clear. Despite studies claiming that type H and the type L endothelium might be associated with differential subsets of

MSCs, evidence is lacking to identify the specific subpopulations of MSCs coupling with and regulating specialized vessel subtypes (Kusumbe et al., 2016; Sivaraj and Adams, 2016; Zhou et al., 2014).

Here, we show that Gli1$^+$ cells represent a subpopulation of MSCs that couple with and regulate type H vessel formation. As the preferable vasculature where Gli1$^+$ cells are adjacently localized, type H capillaries have close functional correlation with Gli1$^+$ cells in bone growth and defect healing processes. Genetic ablation experiments further identified that Gli1$^+$ cells contribute to type H vessel formation which is indispensable for bone homeostasis and healing. In addition, cellular and molecular investigations suggested that Gli and hypoxia inducible factor-1 alpha (HIF-1α) signaling are involved in Gli1$^+$ cell-mediated regulation of angiogenesis. These findings suggest a functional framework that Gli1$^+$ cells drive the formation of the neighboring specialized vasculature for tissue generation and repair.

RESULTS

Gli1$^+$ Cells Are Spatially Coupled with Type H Vessels

While Gli1$^+$ cells contribute to bone homeostasis (Kramann et al., 2015; Schneider et al., 2017; Shi et al., 2017), we hereby use *Gli1-LacZ* mice (Zhao et al., 2015) to characterize the locational correlation between Gli1$^+$ cells and vessels in bone. In the meanwhile, we have used CD105, neuron-glial antigen 2 (NG2), CD146, and stem cell antigen 1 (SCA1) as the putative *in vivo* MSC marker combination (Zhao et al., 2014). We found that Gli1$^+$ cells expressed these markers (Figure 1A), and are located adjacent to CD31$^+$ ECs (Figure 1A), further confirming Gli1$^+$ cell identity as a specific subpopulation of MSCs located in the skeletal perivascular niche (Kramann et al., 2015; Schneider et al., 2017; Shi et al., 2017). Considering that type H vessels are recognized as a specific vessel subtype upstream of type L vessels and supporting skeletal formation and regeneration (Kusumbe et al., 2014; Ramasamy et al., 2014), we hereby focused on the cellular distribution adjacent to distinct types of blood vessels in bone (Figure S1). We first examined the association of the putative *in vivo* MSC markers with type H vessels and observed preferential colocation of these markers with the CD31^{hi}EMCN^{hi} type H endothelium, which were essentially absent from the vicinity of CD31^{lo}EMCN^{lo} type L vessels (Figures 1B–1F), suggesting spatial correlation of MSCs and type H vessels. Notably, further exploration on Gli1$^+$ cells demonstrated that, in the femoral metaphyseal region close to the growth plate, Gli1$^+$ cells preferably resided with type H endothelium (Figure 1G). Quantification analysis also confirmed that metaphyseal Gli1$^+$ cells were distributed particularly close to the type H vasculature, rather than the type L vessels (Figure 1H) (Kusumbe et al., 2014). Furthermore, the selective position of Gli1$^+$ cells around the type H vessels was also identified in the diaphyseal region (Figures 1G and 1H). These findings indicated that Gli1$^+$ cells represented a subpopulation of MSCs that are spatially correlated with type H vessels.

Gli1$^+$ Cells Are Phenotypically Coupled with Type H Vessels in Bone Growth

To investigate whether Gli1$^+$ cells and type H vessels were phenotypically coupled, we took a detailed look at their changes in the bone mass accrual process. We discovered that, in both metaphyseal and diaphyseal regions, there were more Gli1$^+$ cells in juvenile (4-week-old) individuals compared with adult (8-week-old) compartments (Figures 2A–2D), with synergistic changes of type H vessels, rather than the type L vasculature (Figures 2A–2D). Phenotypic correlation of Gli1$^+$ cells and type H vessels were additionally confirmed by flow cytometric analysis, in which the frequencies of both Gli1$^+$ cells and type H ECs in total bone cells dropped in adults (Figure 2E). Similar changes were detected in the putative *in vivo* MSC marker-labeled cells (Figures S2A–S2F). These phenomena were related to declined osteogenesis in the adult bone compared with the juvenile bone (Kusumbe et al., 2014), as verified by the decline of osteoprogenitor marker Runt-related transcription factor 2 (RUNX2) (Figures S2G and S2H). Collectively, these results suggested a specific biological pattern that Gli1$^+$ cells represented a subpopulation of MSCs that were phenotypically coupled with the type H vasculature in bone growth.

Gli1$^+$ Cells Emerge and Guide Type H Vessels in Bone Defect Healing

Next, we examined whether Gli1$^+$ cells and type H vessels were functionally linked. We established a bone defect healing model (Shang et al., 2014), and discovered an outburst appearance of Gli1$^+$ cells in the healing area compared with the undefective adult diaphysis at 2 weeks after the modeling, which was accompanied by a dramatic increase of type H vessels (Figures 3A–3C). Gli1$^+$ cells were also associated with RUNX2-labeled osteoprogenitors in the healing defect region, suggesting participation in the osteogenesis process (Figure 3D). Importantly, the emerged Gli1$^+$ cells were distributed mainly surrounding the type H endothelium (Figures 3A–3C). Quantification analysis confirmed the remarkable upregulation of Gli1$^+$ cells and type H vessels (Figure 3E), as well as the spatial coupling between Gli1$^+$ cells and type H vessels during defect healing (Figure 3F). Similar changes were detected in the putative *in vivo* MSC marker-labeled cells (Figure S3).

To get a clue on how Gli1$^+$ cells and the type H endothelium were correlated, we performed a time course

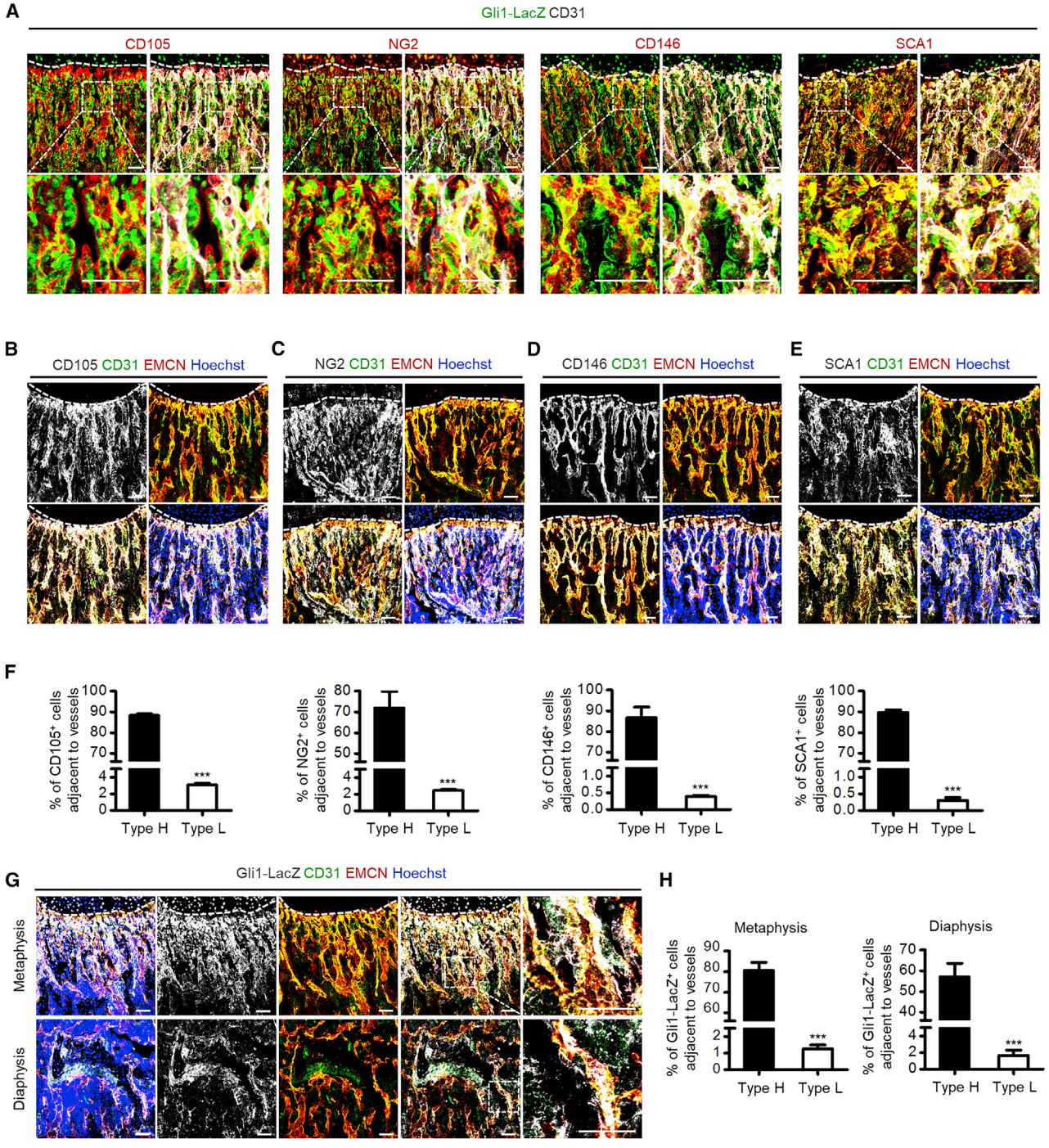

Figure 1. Gli1$^+$ Cells are Spatially Coupled with Type H Vessels in Bone

(A) β-Galactosidase (β-gal) immunostaining showing Gli1-LacZ$^+$ cells (green), CD31 (white), and CD105, NG2, CD146, or SCA1 (red) co-immunostaining in the femoral metaphysis of 4-week-old *Gli1-LacZ* mice. Dotted lines outline margins of growth plates in the metaphysis. The boxed areas are shown magnified in the bottom images. Scale bars, 100 μm.

(B) CD105 (white), CD31 (green), and EMCN (red) co-immunostaining in the femoral metaphysis of 4-week-old *Gli1-LacZ* mice counterstained by Hoechst (blue). Dotted lines outline margins of growth plates in the metaphysis. Scale bars, 100 μm.

(C) NG2 (white), CD31 (green), and EMCN (red) co-immunostaining in the femoral metaphysis of 4-week-old *Gli1-LacZ* mice counterstained by Hoechst (blue). Dotted lines outline margins of growth plates in the metaphysis. Scale bars, 100 μm.

(legend continued on next page)

experiment in which we focused on the early phase of femoral defect healing, e.g., 3, 9, and 24 h, and 3 and 7 days, after establishment of the defect model, according to previous studies (Chen et al., 2007; Wallner et al., 2016). As shown, as early as 9 h after defect modeling, Gli1$^+$ cells appeared in the granulated tissue, while type H vessels emerged at the edge of the defect region (Figure 3G). At 24 h and 3 days, type H vessels grew toward the healing area, and at 7 days both Gli1$^+$ cells and the type H endothelium were abundant in the healing defect region (Figure 3G). Statistical analysis confirmed the significant upregulation of Gli1$^+$ cells and type H vessels in the early time course of bone healing, during which changes of Gli1$^+$ cells occurred before type H vessels (Figure 3H). Notably, the fold change of type H vessel density could reach to higher than 25, while that of type L vessel density stayed lower than 4 (Figure 3H), indicating substantial formation of type H vessels. These data indicated that Gli1$^+$ cells emerge and guide the type H vasculature formation in bone healing.

Gli1$^+$ Cells Are Indispensable for Type H Vessel Formation in Bone Growth

To decipher whether Gli1$^+$ cells indeed regulated the angiogenesis of type H vessels, we generated *Gli1-CreER^{T2};iDTA* mice and injected them with tamoxifen at one month of age (Figure 4A). As proved previously (Zhao et al., 2015), tamoxifen administration caused successful ablation of Gli1$^+$ cells in bone, which was verified by quantitative real-time PCR and western blotting analyses (Figure S4A and S4B). Similarly, cells labeled by the putative *in vivo* MSC markers were significantly reduced (Figures 4B and 4C and Figure S4C–S4F). Four days after the last dose of tamoxifen injection, we observed a sharp decline of type H vessels in both the metaphyseal and the diaphyseal regions, suggesting the sensitivity of the type H endothelium to Gli1$^+$ cell alterations (Figures 4D–4G). Type L vessels, on the other hand, showed upregulation, which was a kind of compensatory behavior taking over the original place of type H vessels (Figures 4D–4G). The dramatic decline of type H vessels was further accompanied by remarkable loss of RUNX2$^+$ osteoprogenitors (Figures 4D–4G), leading to inhibition of bone mass accrual (Figure S5A) with reduced bone volume over tissue volume (BV/TV) and trabecular numbers (Tb.N) after Gli1$^+$ cell ablation (Figure S5B). Furthermore, the HIF-1α pathway has been reported to coordinate angiogenesis during skeletal development and promote type H vessel formation in postnatal bone while the cellular origin remains unclear (Kusumbe et al., 2014; Wang et al., 2007). In this regard, we explored the changes of HIF-1α expression and found that Gli1$^+$ cell ablation led to significant suppression of HIF-1α signaling (Figure 4H), suggesting that HIF-1α signaling was regulated by Gli1$^+$ cells, which might underlie Gli1$^+$ cell-mediated modulation of type H vessels.

Genetic Ablation of Gli1$^+$ Cells Leads to Reduced Type H Vessels during Bone Healing

Next, we investigated the functional importance of Gli1$^+$ cell-mediated regulation of type H vessel formation in bone healing by establishing femoral defect model in *Gli1-CreER^{T2};iDTA* mice (Figure 5A). Data demonstrated that Gli1$^+$ cell ablation led to dramatic suppression of the putative *in vivo* MSC markers in healing defects (Figures 5B and 5C), supporting the efficacy of Gli1$^+$ cell deletion. As to the changes of type H vessels, during the early phase of femoral defect healing, e.g., 9 and 24 h after defect modeling, Gli1$^+$ cell ablation significantly inhibited the growth of type H vessels toward the healing area (Figure 5D). We then made further analysis at 3 weeks after defect when, according to previous results, there was an outburst co-appearance of Gli1$^+$ cells and type H vessels in wild-type mice. Results revealed that loss of Gli1$^+$ cells significantly impaired type H vessel upregulation in the defect region during healing, with diminished RUNX2$^+$ osteoprogenitors (Figure 5E). Statistical analysis further confirmed Gli1$^+$ cell ablation-mediated inhibition of type H vessel formation (Figures 5F and 5G). Also, the expression of HIF-1α was diminished in the defect region during healing (Figure 5H). As a result, loss of Gli1$^+$ cells remarkably repressed bone defect healing (Figure S5C), as proved by reduced BV/TV and Tb.N in the healing defect area

(D) CD146 (white), CD31 (green), and EMCN (red) co-immunostaining in the femoral metaphysis of 4-week-old *Gli1-LacZ* mice counterstained by Hoechst (blue). Dotted lines outline margins of growth plates in the metaphysis. Scale bars, 100 μm.
(E) SCA1 (white), CD31 (green), and EMCN (red) co-immunostaining in the femoral metaphysis of 4-week-old *Gli1-LacZ* mice counterstained by Hoechst (blue). Dotted lines outline margins of growth plates in the metaphysis. Scale bars, 100 μm.
(F) Quantification of percentages of CD105$^+$, NG2$^+$, CD146$^+$, and SCA1$^+$ cells adjacent to type H and type L vessels. n = 3 mice per group.
(G) β-Gal immunostaining showing Gli1-LacZ$^+$ cells (white) with CD31 (green) and EMCN (red) co-immunostaining in the femoral metaphysis and diaphysis of 4-week-old *Gli1-LacZ* mice counterstained by Hoechst (blue). Dotted lines outline margins of growth plates in the metaphysis. The boxed areas are shown magnified on the right. Scale bars, 100 μm.
(H) Quantification of percentages of Gli1-LacZ$^+$ cells adjacent to type H and type L vessels in the metaphysis and diaphysis of 4-week-old *Gli1-LacZ* mice. n = 5 mice per group.
***p < 0.0001. Data are presented as mean ± SD. See also Figure S1.

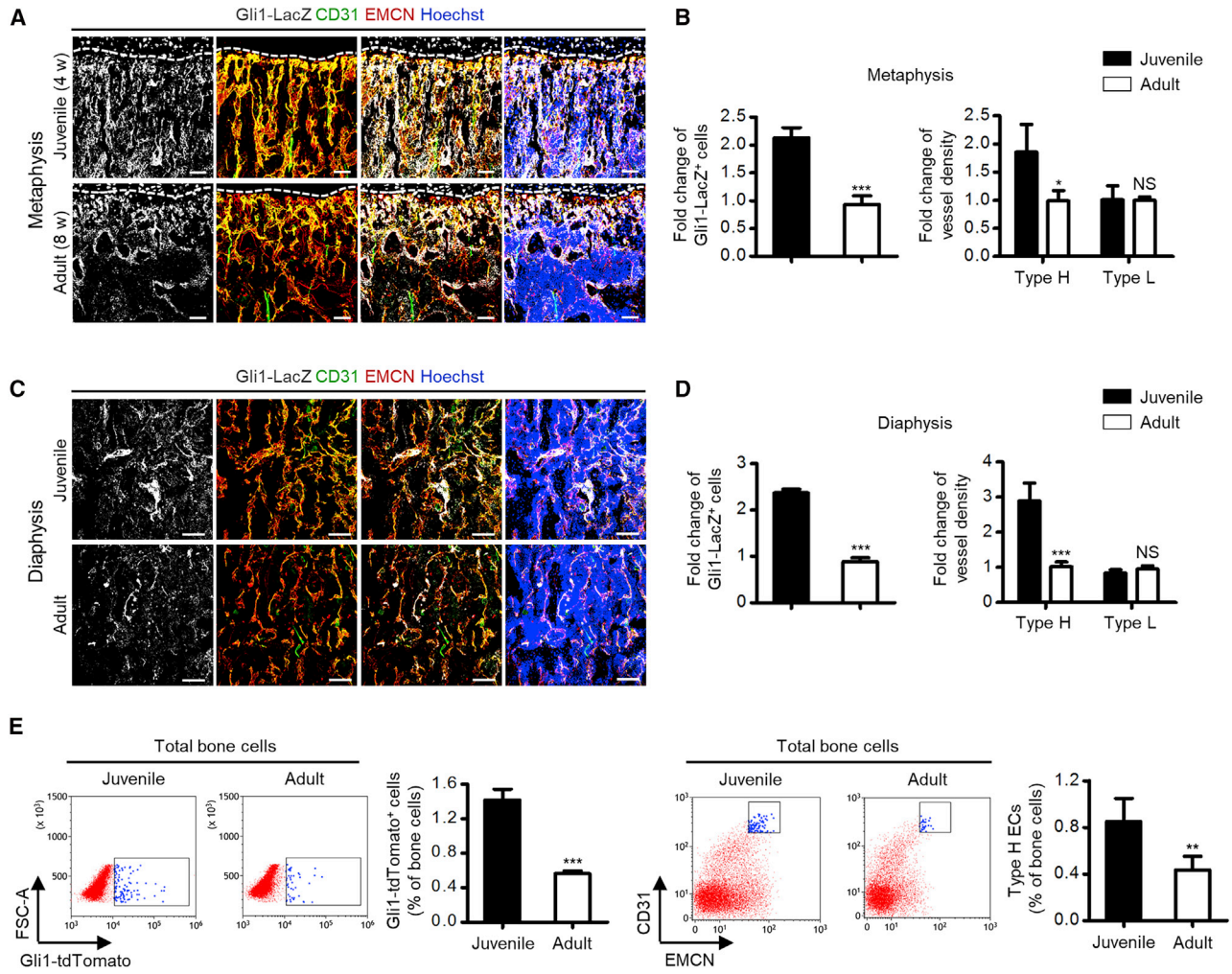

Figure 2. Gli1$^+$ Cells are Phenotypically Coupled with Type H Vessels in Bone Growth

(A) β-Gal immunostaining showing Gli1-LacZ$^+$ cells (white) with CD31 (green) and EMCN (red) co-immunostaining in the femoral metaphysis of juvenile (4-week old) and adult (8-week old) *Gli1-LacZ* mice counterstained by Hoechst (blue). Dotted lines outline margins of growth plates in the metaphysis. Scale bars, 100 μm.

(B) Quantification of fold changes of Gli1-LacZ$^+$ cells, type H vessels, and type L vessels in the metaphysis of juvenile and adult *Gli1-LacZ* mice. n = 4 mice per group.

(C) β-Gal immunostaining showing Gli1-LacZ$^+$ cells (white) with CD31 (green) and EMCN (red) co-immunostaining in the femoral diaphysis of juvenile and adult *Gli1-LacZ* mice counterstained by Hoechst (blue). Scale bars, 100 μm.

(D) Quantification of fold changes of Gli1-LacZ$^+$ cells, type H vessels, and type L vessels in the diaphysis of juvenile and adult *Gli1-LacZ* mice. n = 4 mice per group.

(E) Flow cytometric analysis of percentages of Gli1-tdTomato$^+$ cells in total bone cells of juvenile and adult bigenic *Gli1-CreER^{T2};mT/mG* mice receiving tamoxifen (100 μg/g i.p. daily, three times; mice sacrificed 3 days after the last injection), and percentages of CD31^{hi}EMCN^{hi} type H ECs in total bone cells of juvenile and adult mice. n = 5 mice per group.

*p < 0.05, **p < 0.01, ***p < 0.0001; NS, p > 0.05. Data are presented as mean ± SD. See also Figure S2.

(Figure S5D). The above findings together indicated that Gli1$^+$ cells were indispensable for type H vessel formation to promote bone regeneration. Moreover, we also investigated the effects of Gli1$^+$ cell deletion on skin, which possesses abundant vessels and depends on angiogenesis for wound healing. We established a cutaneous wound healing model in *Gli1-CreER^{T2};iDTA* mice and detected the changes of type H vessels. Compared with control mice, loss of Gli1$^+$ cells inhibited the repair of the wound and the formation of type H vessels in the wound healing area (Figure S6), further supporting the role of Gli1$^+$ cells in promoting regenerative type H vessel formation.

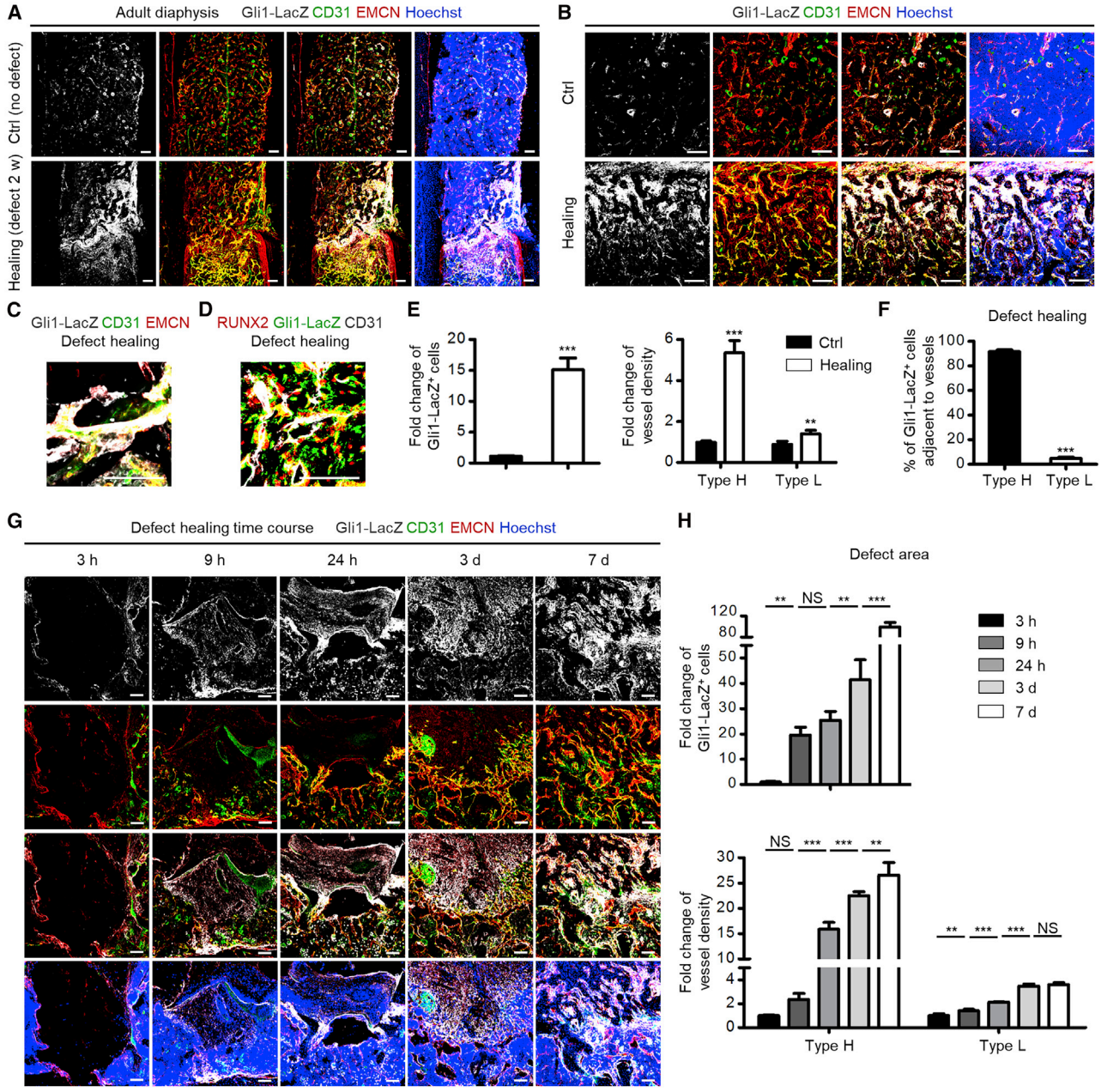

Figure 3. Gli1$^+$ Cells Emerge and Guide Type H Vessels in Bone Defect Healing

(A) β-Gal immunostaining showing Gli1-LacZ$^+$ cells (white) with CD31 (green) and EMCN (red) co-immunostaining in femoral diaphysis from 10-week-old *Gli1-LacZ* mice without defects (Ctrl) or with healing defects at 2 weeks after femoral defect modeling counterstained by Hoechst (blue). Scale bars, 100 μm.

(B) β-Gal immunostaining showing Gli1-LacZ$^+$ cells (white) with CD31 (green) and EMCN (red) co-immunostaining in non-defective (Ctrl mice) or defect healing area (mice with defect modeling) counterstained by Hoechst (blue). Scale bars, 100 μm.

(C) Representative β-gal immunostaining showing Gli1-LacZ$^+$ cells (white) with CD31 (green) and EMCN (red) co-immunostaining in healing defect areas of *Gli1-LacZ* mice counterstained by Hoechst (blue). Scale bars, 100 μm.

(D) Representative β-gal immunostaining showing Gli1-LacZ$^+$ cells (green) with co-immunostaining of CD31 (white) and osteogenic marker RUNX2 (red) in healing defect areas of *Gli1-LacZ* mice counterstained by Hoechst (blue). Scale bars, 100 μm.

(E) Quantification of fold changes of Gli1-LacZ$^+$ cells, type H vessels, and type L vessels in Ctrl and healing area at 2 weeks after femoral defect modeling. n = 3–4 mice per group.

(legend continued on next page)

Gli1$^+$ Cells through HIF-1α Signaling Regulate Endothelial Angiogenesis

To directly evaluate whether Gli1$^+$ cells were responsible for promoting angiogenesis and to dissect the molecular basis of Gli1$^+$ cell-mediated regulation of type H vessels, we performed the *in vitro* tube formation assay (Xie et al., 2014). We discovered that co-culture with bone marrow MSCs indeed improved tube and branch formation of ECs, whereas the effects were barely detected when using MSCs isolated from Gli1$^+$ cell ablated mice that lack the subpopulation of Gli1$^+$ cells (Figures 6A and 6B), suggesting that Gli1$^+$ cells are indispensable for regulating endothelial angiogenesis. Besides, the pro-angiogenic effects of MSCs were significantly restrained by pretreating MSCs with Gli antagonist 61 (GANT61), a specific Gli protein inhibitor (Schneider et al., 2017) (Figures 6A and 6B), which indicated involvement of Gli signaling in Gli1$^+$ cell-mediated angiogenic regulation. Furthermore, we explored the involvement of the HIF-1α pathway by pretreating MSCs with deferoxamine mesylate (DFM), which enhances stability and activity of HIF-1α (Kusumbe et al., 2014), and PX-478, an inhibitor of HIF-1α (Agarwal et al., 2016), respectively. Results demonstrated that DFM pretreatment improved the effects of MSCs on promoting angiogenesis, while PX-478 showed suppressive action (Figures 6C and 6D). More importantly, further experiments confirmed that, for MSCs isolated from Gli1$^+$ cell-depleted mice, DFM pretreatment failed to improve the pro-angiogenic effects, indicating that HIF-1α signaling plays a role in mediating the pro-angiogenic effects of Gli1$^+$ cells (Figures 6E and 6F). Collectively, the evidence suggested that Gli1$^+$ cells, through Gli and HIF-1α signaling, contributed to type H vessel angiogenesis (Figure 6G).

DISCUSSION

Postnatal MSCs reside in the perivascular niche, maintain tissue homeostasis, and safeguard tissue repair, whereas little is known about whether and how their perivascular localization and angiogenesis-regulatory function are linked (Crisan et al., 2008; Kfoury and Scadden, 2015; Lemos and Duffield, 2018). Gli1 identifies a subpopulation of MSCs particularly in bone (Kramann et al., 2015; Schneider et al., 2017; Shi et al., 2017), where the specialized type H vessels have been recently recognized to support skeletal formation and regeneration (Kusumbe et al., 2014; Ramasamy et al., 2014; Xu et al., 2018). In this study, we discovered that Gli1$^+$ cells were preferentially localized adjacent to type H vessels in bone; Gli1$^+$ cells and type H vessels further possessed close functional correlation in the bone growth and defect healing processes. Importantly, Gli1$^+$ cells were revealed to be essential for type H vessel formation in bone homeostasis and healing. These findings suggest a functional framework that the Gli1$^+$ subpopulation of MSCs drives formation of the coupled specialized vasculature for tissue generation and repair.

Postnatal MSCs play a role in tissue homeostasis, the *in vivo* identity of which associated with their specific function remains as a research focus (Kfoury and Scadden, 2015; Lemos and Duffield, 2018). Particularly in bone, a typical reservoir of MSCs, lineage-tracing studies have indicated subpopulations of MSCs marked by Nestin, Leptin receptor (LepR), among others, mediating skeletal and hematopoietic maintenance (Mendez-Ferrer et al., 2010; Zhou et al., 2014). Among them, Gli1 especially defines a subpopulation of MSCs characterized by perivascular location which contribute to bone formation and injury repair (Kramann et al., 2015; Schneider et al., 2017; Shi et al., 2017). Accordingly, targeting skeletal MSCs to facilitate bone regeneration holds promise for counteracting bone loss and promoting defect and fracture healing (Sui et al., 2019; Zheng et al., 2019). In this study, we revealed that Gli1$^+$ cells, which expressed the putative *in vivo* MSC markers, are upstream of specialized type H vessels. The type H vessels are identified with distinct functional properties to couple angiogenesis to osteogenesis and mediate bone generation (Kusumbe et al., 2014; Ramasamy et al., 2014). Anatomically, arteries exclusively connect to type H vessels in the metaphysis and endosteum while they do not deliver blood directly into type L sinusoidal capillaries. Thus distinct trophic and oxygenous microenvironments can be detected in different vascular regions of the postnatal long bone (Kusumbe et al., 2014; Ramasamy et al., 2014). Consequently, the type H vasculature, together with the released growth factors by type H ECs, supports an appropriate niche for osteoprogenitors in skeletal growth and repair (Kusumbe et al., 2014; Ramasamy et al., 2014; Xu et al., 2018). In this study, we unraveled an intriguing role of Gli1$^+$ cells to guide and initiate type H vessel angiogenesis during bone growth and healing.

(F) Quantification of percentages of Gli1$^+$ cells adjacent to type H and type L vessels in healing areas at 2 weeks after femoral defect modeling. n = 3–4 mice per group.

(G) β-Gal immunostaining showing Gli1-LacZ$^+$ cells (white) with CD31 (green) and EMCN (red) co-immunostaining in healing defect areas of *Gli1-LacZ* mice at indicated time points after femoral defect modeling counterstained by Hoechst (blue). Scale bars, 100 μm.

(H) Quantification of fold changes of Gli1-LacZ$^+$ cells, type H vessels, and type L vessels in healing area during the healing time course. n = 3 mice per group.

$^{**}p < 0.01$; $^{***}p < 0.0001$; NS, $p > 0.05$. Data are presented as mean ± SD. See also Figure S3.

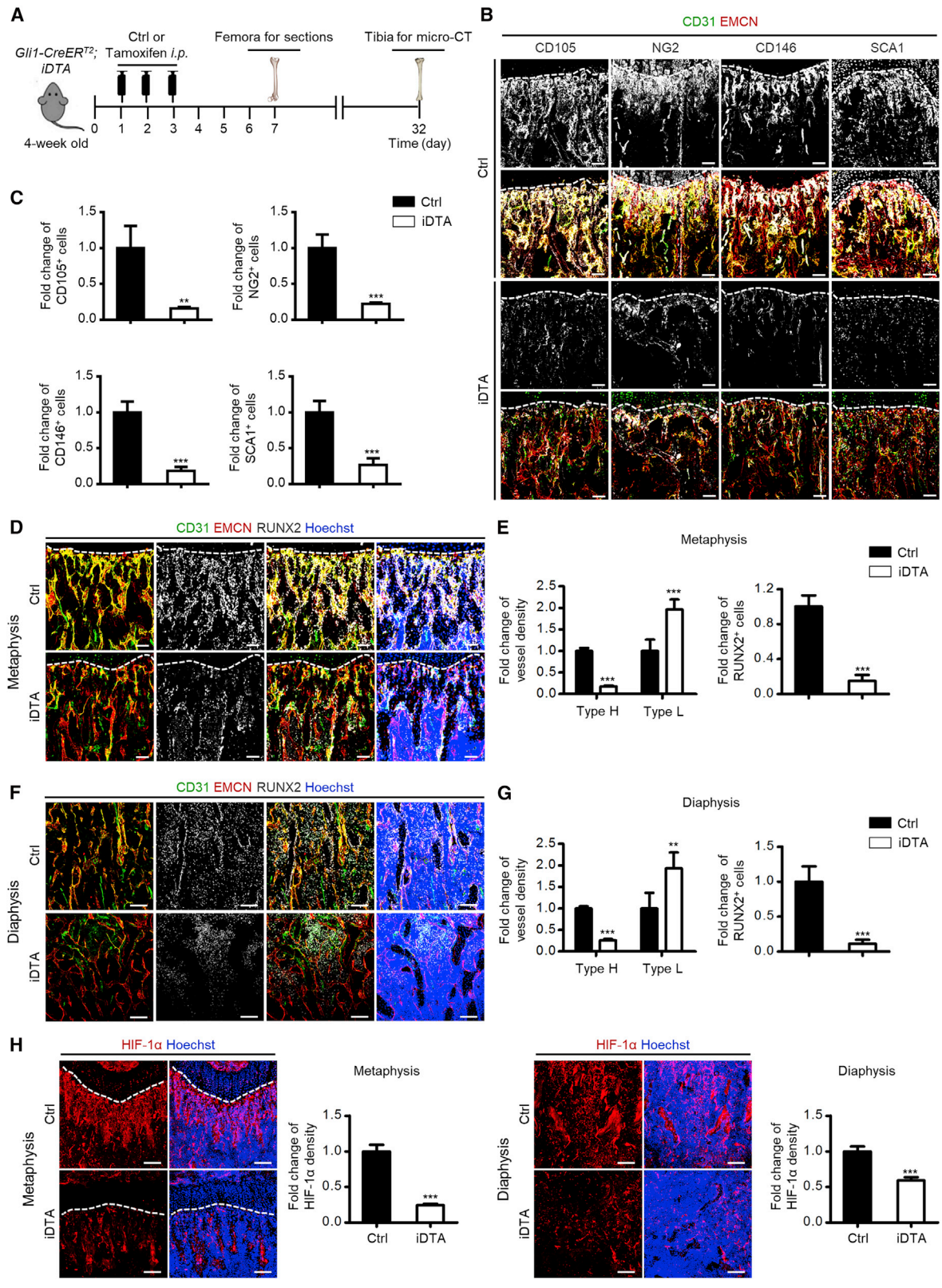

(legend on next page)

Besides, we also revealed that Gli1$^+$ cells were essential for type H vessel formation in skin wound healing which depends on angiogenesis for regenerative repair. Considering that Gli1$^+$ cells exist in multiple organs (Kramann et al., 2015) and different organs have heterogeneous vasculature (Kalucka et al., 2020), it remains interesting to investigate whether MSC-mediated regulation of specialized angiogenesis underlies tissue development and regeneration across the organism. In addition, Gli1$^+$ cells have been identified as MSCs in human bone marrow via immunostaining and *in vitro* culture, comparable with the findings in murine bone marrow. More importantly, Gli1$^+$ cells were revealed to expand in patients with bone marrow fibrosis, which could be targeted therapeutically (Schneider et al., 2017). Also, Gli1$^+$ cells were found to be located in the arterial adventitia in human kidney and associated with vascular calcification of patients with chronic kidney disease (Kramann et al., 2016), further indicating that Gli1 is also a useful marker for human MSCs and thus provides a promising target for stem cell-based therapies.

Accumulating findings highlight a perivascular origin of MSCs in broad tissue/organ distribution, despite evidence challenging pericytes as multipotent tissue-resident progenitors (Crisan et al., 2008; Guimaraes-Camboa et al., 2017; Shi and Gronthos, 2003). Functionally, the perivascular Gli1$^+$ cells, especially those in the skeletal system (Kramann et al., 2015; Shi et al., 2017; Zhao et al., 2015), have been documented as critical contributors to organ development and injury repair (Schneider et al., 2017; Shi et al., 2017; Zhao et al., 2015), both of which depend on the vascular system to transport oxygen, nutrients, and circulating cells, as well as carry away waste products (Butler et al., 2010; Red-Horse et al., 2007). Despite the fact that a number of reports on *in vitro* and regenerative applications have shown the promotion of angiogenesis by MSCs (Kasper et al., 2007; Manieri et al., 2015), it remains poorly understood *in situ* whether MSCs regulate angiogenesis in the perivascular niche. In this study, we revealed that Gli1$^+$ cells initiated the neighboring type H vessel angiogenesis in bone growth and healing, therefore providing fundamental insights into the positional-functional correlations of perivascular MSCs. Furthermore, this specific angiogenic regulation may create a distinct metabolic and molecular microenvironment, thus benefiting osteoprogenitors for bone homeostatic maintenance and regenerative repair (Kusumbe et al., 2014; Xu et al., 2018), which further provides mechanistic insights into the bone generation and regeneration processes.

Elucidating cellular and molecular mechanisms regulating type H vessel angiogenesis is of much value for developing approaches to counteract bone loss and enhance bone healing (Kusumbe et al., 2014; Xu et al., 2018). Originally established, type H vessel growth is facilitated by angiocrine release of Noggin regulated by endothelial Notch activity, which is maintained by the miR-497–195 cluster (Ramasamy et al., 2014; Yang et al., 2017). Later on, angiogenic factors secreted by osteoblasts and preosteoclasts, such as C-X-C motif chemokine ligand 9 (CXCL9), Slit homolog 3, and platelet-derived growth factor-BB, have been documented to promote the formation of type H vasculature (Huang et al., 2016; Xie et al., 2014; Xu et al., 2018). The above angiogenic proteins have shown pharmacological potential as osteoanabolic therapies. In addition, a recent study has reported that intermittent parathyroid hormone treatment expands type H ECs and mobilizes perivascular LepR$^+$ cells, indicating extrinsic hormonal regulation of type H vessels in relation to MSC-based anti-osteoporotic actions (Caire et al., 2019). Recent studies have also indicated that distinct MSC subsets reside adjacent to type H or type L vessels (Sivaraj and Adams, 2016), e.g., platelet-derived growth factor receptor beta (PDGFRβ)$^+$ and NG2$^+$ subpopulations are associated

Figure 4. Gli1$^+$ Cells are Indispensable for Type H Vessel Formation in Bone Growth

(A) Schematic diagram showing experimental design to analyze skeletal effects of Gli1$^+$ cell ablation.

(B) CD31 (green), EMCN (red), and the putative *in vivo* MSC markers (white) co-immunostaining in the femoral metaphysis of Ctrl and Gli1$^+$ cell ablated mice. Dotted lines outline margins of growth plates in the metaphysis. Scale bars, 100 μm.

(C) Quantification of fold changes of CD105$^+$, NG2$^+$, CD146$^+$, and SCA1$^+$ cells in the metaphysis of Ctrl mice against Gli1$^+$ cell ablated mice. n = 3–4 mice per group.

(D) CD31 (green), EMCN (red), and RUNX2 (white) co-immunostaining in the femoral metaphysis of Ctrl and Gli1$^+$ cell ablated mice counterstained by Hoechst (blue). Dotted lines outline margins of growth plates in the metaphysis. Scale bars, 100 μm.

(E) Quantification of fold changes of type H vessels, type L vessels, and RUNX2$^+$ cells in the metaphysis of Ctrl against Gli1$^+$ cell ablated mice. n = 6 mice per group.

(F) CD31 (green), EMCN (red), and RUNX2 (white) co-immunostaining in femoral diaphysis of Ctrl and Gli1$^+$ cell ablated mice counterstained by Hoechst (blue). Scale bars, 100 μm.

(G) Quantification of fold changes of type H vessels, type L vessels, and RUNX2$^+$ cells in the diaphysis of Ctrl against Gli1$^+$ cell ablated mice. n = 6 mice per group.

(H) HIF-1α (red) immunostaining in the femoral metaphysis and diaphysis of Ctrl and Gli1$^+$ cell ablated mice counterstained by Hoechst (blue). Dotted lines outline margins of growth plates in the metaphysis. Scale bars, 100 μm. Quantification of fold changes of HIF-1α in the metaphysis and diaphysis of Ctrl against Gli1$^+$ cell ablated mice. n = 3 mice per group.

$^{**}p < 0.01$, $^{***}p < 0.0001$. Data are presented as mean ± SD. See also Figures S4 and S5.

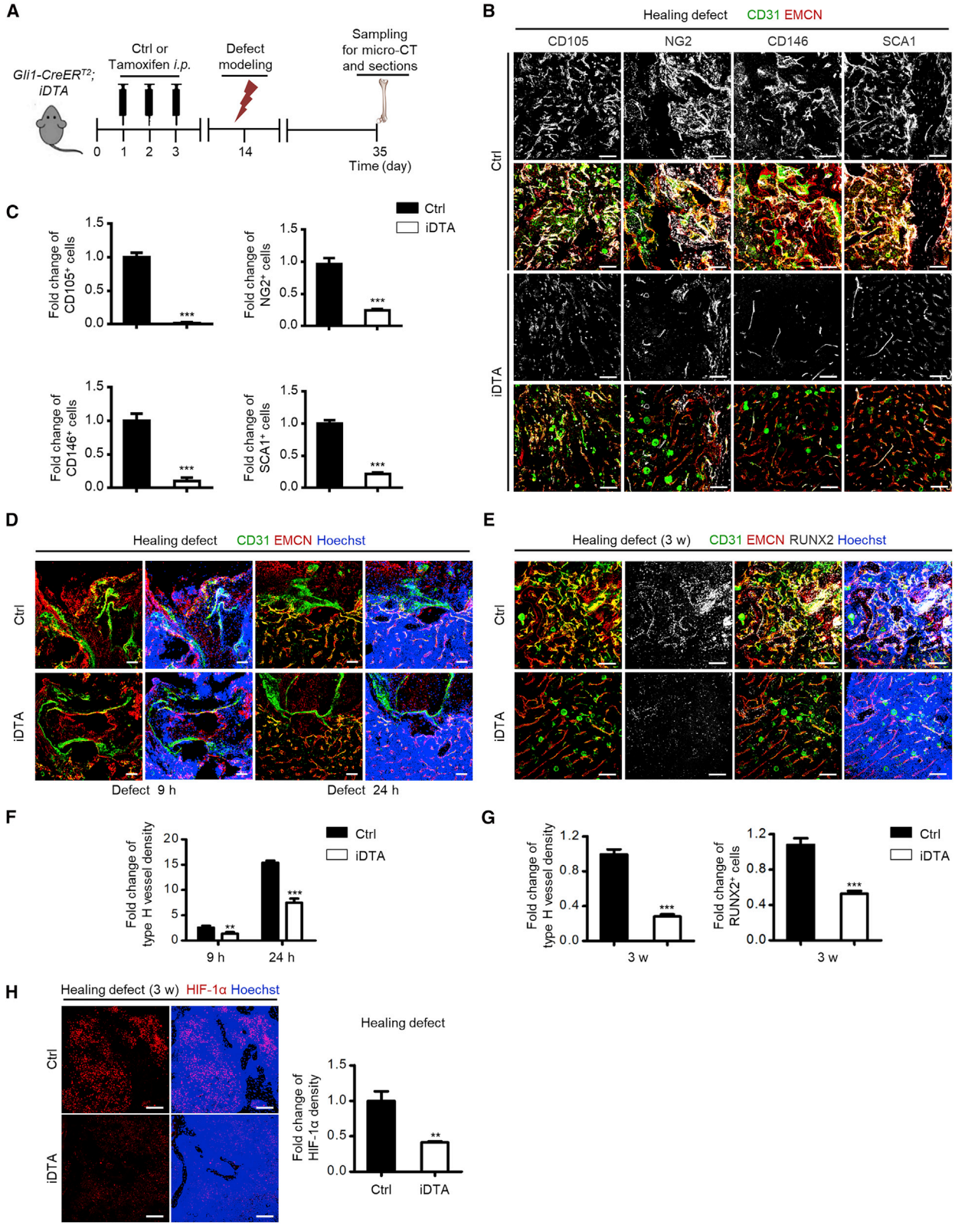

(legend on next page)

with the type H vasculature (Kusumbe et al., 2016), while the type L sinusoids are surrounded by subpopulations expressing LepR and CXCL12 (Ding et al., 2012; Sugiyama et al., 2006). Nevertheless, while evidence has revealed functional properties of distinct MSC subsets in the regulation of hematopoiesis and osteogenesis, their roles in maintaining vascular homeostasis in relation to their specific locations are less clear (Sivaraj and Adams, 2016; Sugiyama et al., 2006; Zhou et al., 2014). In this study, at the stem cell level, we further revealed that Gli1$^+$ cells promote type H vessel angiogenesis during development and regenerative repair, which integrates into the current picture of type H vessel regulation and suggests promising targets for stem cell-based, vasculature-targeted bone regeneration therapies.

Gli proteins are a family of zinc finger transcription factors (Jiang and Hui, 2008) that respond to the hedgehog (HH) signaling pathway and contribute to MSC maintenance (Shi et al., 2017; Zhao et al., 2014, 2015), e.g., in the adult mouse incisor the released Sonic hedgehog (SHH) protein activates Gli1 expression to safeguard MSC homeostasis (Zhao et al., 2014). Accordingly, targeted inhibition of Gli signaling by GANT61 (reported here and by others) attenuates MSC properties (Schneider et al., 2017). Through application of GANT61, we further revealed that Gli signaling is involved in the MSC-mediated regulation of angiogenesis. It has also been reported that HIF-1α signaling couples angiogenesis to osteogenesis during skeletal development (Ramasamy et al., 2014; Wang et al., 2007), while HIF-1α also triggers responses of HH signaling and Gli1 protein (Bijlsma et al., 2009; Lei et al., 2015). Previous studies have shown that systemic administration of DFM upregulates type H vessels in bone, and that endothelial HIF-1α signaling promotes type H vessel formation (Kusumbe et al., 2014; Yang et al., 2017). In this study, we revealed that Gli1$^+$ cell ablation led to significant downregulation of HIF-1α expression in both bone growth and regeneration, which suggests that Gli1$^+$ cells are an important cellular source of HIF-1α signaling. In addition, despite the lack of a Gli1$^+$ cell subpopulation, MSCs derived from Gli1$^+$ cell ablated mice could still be cultured *in vitro*, suggesting that Gli1$^+$ cells exert little effects on the proliferation of MSCs. Nevertheless, the positive effects of DFM on stimulating angiogenesis were significantly restrained, indicating that Gli1$^+$ cells represented the critical cellular basis of HIF-1α-mediated type H vessel angiogenesis. Future studies will address the detailed mechanisms underlying the effects of Gli1$^+$ cell-derived HIF-1α signaling on the type H endothelium, which might be due to the regulation of vascular endothelial growth factor expression (Wang et al., 2007). It remains interesting to evaluate whether the molecular targets of these processes can be used to prevent tissue degeneration or promote regenerative tissue healing.

In summary, Gli1$^+$ cells represent a subpopulation of postnatal MSCs to guide and initiate the formation of neighbored specialized type H vasculature, which supports skeletal development and regeneration. Our findings implicate a link between perivascular localization of MSCs and their angiogenesis-regulatory function, paving the way for stem cell-based, vasculature-targeted osteoanabolic therapies.

EXPERIMENTAL PROCEDURES

Study Approval

All animal experiments were performed in compliance with the relevant laws and institutional guidelines of the Fourth Military Medical University for Intramural Animal Use and Care Committee and were approved by local animal ethics committees.

Figure 5. Genetic Ablation of Gli1$^+$ Cells Leads to Reduced Type H Vessels during Bone Healing

(A) Schematic diagram showing experimental design to analyze bone defect healing after Gli1$^+$ cell ablation.

(B) CD31 (green), EMCN (red), and putative *in vivo* MSC markers (white) co-immunostaining in healing defect areas of Ctrl and Gli1$^+$ cell ablated mice. Scale bars, 100 μm.

(C) Quantification of fold changes of CD105$^+$, NG2$^+$, CD146$^+$, and SCA1$^+$ cells in healing defect areas of Ctrl and Gli1$^+$ cell ablated mice. n = 3–4 mice per group.

(D) CD31 (green) and EMCN (red) co-immunostaining in healing defect areas of Ctrl and Gli1$^+$ cell ablated mice at 9 and 24 h after femoral defect modeling counterstained by Hoechst (blue). Scale bars, 100 μm.

(E) CD31 (green), EMCN (red), and RUNX2 (white) co-immunostaining in healing defect areas of Ctrl and Gli1$^+$ cell ablated mice at 3 weeks after femoral defect modeling counterstained by Hoechst (blue). Scale bars, 100 μm.

(F) Quantification of fold changes of type H vessels in healing defect areas of Ctrl against Gli1$^+$ cell ablated mice at 9 and 24 h after femoral defect modeling. n = 3 mice per group.

(G) Quantification of fold changes of type H vessels and RUNX2$^+$ cells in healing defect areas of Ctrl against Gli1$^+$ cell ablated mice at 3 weeks after femoral defect modeling. n = 4–5 mice per group.

(H) HIF-1α (red) immunostaining in healing defect areas of Ctrl and Gli1$^+$ cell ablated mice at 3 weeks after femoral defect modeling counterstained by Hoechst (blue). Scale bars, 100 μm. Quantification of fold changes of HIF-1α in healing defect areas of Ctrl against Gli1$^+$ cell ablated mice. n = 3 mice per group.

$^{**}p < 0.01$, $^{***}p < 0.0001$. Data are presented as mean ± SD. See also Figures S5 and S6.

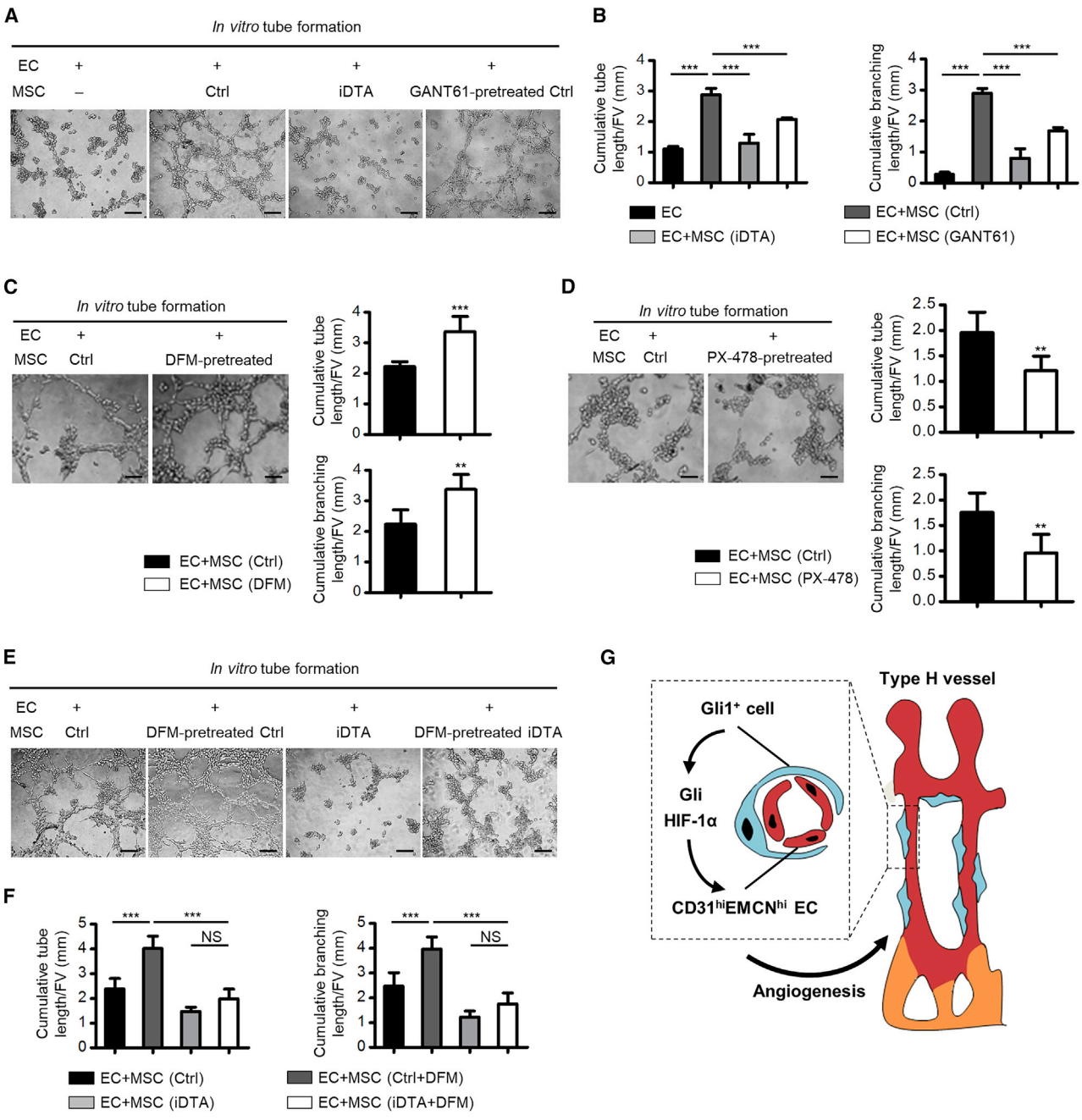

Figure 6. Gli1$^+$ Cells through HIF-1α Signaling Regulate Endothelial Angiogenesis

(A) *In vitro* tube formation by EC, EC co-cultured with MSCs from Ctrl mice, EC co-cultured with MSCs from Gli1$^+$ cell ablated mice, and EC co-cultured with GANT61 (10 μM for 48 h, Gli signaling inhibition)-pretreated MSCs. Scale bars, 100 μm.

(B) Quantification of cumulative tube and branching lengths. n = 4 independent experiments.

(C) *In vitro* tube formation by EC co-cultured with MSCs from Ctrl mice and EC co-cultured with DFM (10 μM for 48 h, HIF-1α stabilizer and activator)-pretreated MSCs. Scale bars, 100 μm. Cumulative tube and branching lengths were quantified. n = 5 independent experiments.

(D) *In vitro* tube formation by EC co-cultured with MSCs from Ctrl mice and EC co-cultured with PX-478 (10 μM for 48 h, HIF-1α inhibitor)-pretreated MSCs. Scale bars, 100 μm. Cumulative tube and branching lengths were quantified. n = 5 independent experiments.

(legend continued on next page)

Animals

The following mouse strains were obtained from the Jackson Laboratory: *Gli1-LacZ* (JAX no. 008211) (Zhao et al., 2015), *Gli1-CreER^{T2}* (JAX no. 007913) (Schneider et al., 2017), *ROSA26-eGFP-DTA* (JAX no. 006331) (Ivanova et al., 2005), and *ROSA26*-mT/mG (JAX no. 007676) (Wang et al., 2018). C57BL/6J mice (JAX no. 000664) were used as the wild type. All mice were housed in a pathogen-free condition, maintained on the standard 12-h light-dark cycle, fed with food and water *at libitum*, and used for analyses regardless of sex. Genotyping was performed by PCR as indicated (Chen et al., 2016; Hu et al., 2017), using tail samples from mice and primer sequences provided by the Jackson Laboratory.

For tracing of Gli1$^+$ cells in bone histology, *Gli1-LacZ* mice were used at the age of 3–6 weeks (juvenile) and 7–12 weeks (adult) (Kusumbe et al., 2014). For tracing of bone marrow Gli1$^+$ cells in flow cytometry, *Gli1-CreER^{T2}* and *ROSA26*-mT/mG transgenics were interbred. For the ablation experiments, *Gli1-CreER^{T2}* and *ROSA26-eGFP-DTA* transgenics were interbred (Zhao et al., 2015). Cre activities were induced by tamoxifen (Sigma-Aldrich), which was dissolved in corn oil and injected intraperitoneally into offspring at 100 μg/g of body weight every day for 3 days (Ramasamy et al., 2014). For bone defect modeling, defects of 0.7 mm in diameter and approximately two-thirds of the femoral diameter in depth (the other side of the cortical bone remains undamaged) were made in the diaphyseal femoral region using columnar dental diamond burs under general anesthesia (Shang et al., 2014). For skin wound modeling, full-layer cutaneous wounds (10 mm in diameter) were carefully made on the dorsal skin using ophthalmic scissors under general anesthesia (Zhao et al., 2017).

Bone Histology and Immunohistochemistry

Freshly dissected femora were collected and fixed in 4% paraformaldehyde (Sigma-Aldrich, USA) solution for 4 h at 4°C. Decalcification was performed with 0.5 M ethylenediaminetetraacetic acid (MP Biomedicals, USA) under constant shaking for 24 h at 4°C, as described (Kusumbe et al., 2015). Decalcified bone samples were then immersed into 30% sucrose (MP Biomedicals, USA) solution for 24 h, embedded, and frozen in optimum cutting temperature compound, and cryosectioned on a Leica cryostat to get 30-μm-thick sections (CM1950, Leica, Germany).

For immunostaining (Ramasamy et al., 2014; Sui et al., 2016), sections were air-dried, permeabilized in 0.3% Triton X-100 (Sigma-Aldrich, USA) for 20 min, blocked in 5% serum (Sigma-Aldrich, USA) at room temperature for 30 min, and probed with the primary antibodies diluted in blocking serum overnight at 4°C. The primary antibodies were β-galactosidase (ab9361, Abcam, UK; diluted 1:200), CD31 (FAB3628G, R&D Systems, USA; diluted 1:100), EMCN (sc-65495, Santa Cruz Biotechnology, USA; diluted 1:100), CD105 (MAB1320, R&D Systems, USA; diluted 1:100), NG2 (ab5320, Millipore, USA; diluted 1:100), CD146 (ab75769, Abcam, UK; diluted 1:100), SCA1 (ab51317, Abcam, UK; diluted 1:200), RUNX2 (12556, Cell Signaling Technology, USA; diluted 1:200), and HIF-1α (ab179483, Abcam, UK; diluted 1:100). After primary antibody incubation, sections were washed with PBS three times and incubated with appropriate Alexa Fluor-conjugated secondary antibodies (Molecular Probes, USA; diluted 1:400) for 1 h at room temperature. Sections were then washed with PBS three times and nuclei were counterstained with Hoechst 33342 (Sigma-Aldrich, USA) for 30 min at room temperature. After counterstaining, sections were washed with PBS three times and mounted by propanetriol (Sigma-Aldrich, USA).

Image Acquisition and Quantitative Analysis

Immunofluorescent staining sections were analyzed using an Olympus laser scanning confocal microscope (FV1000, Olympus, Japan). z stacks of images were scanned at high resolution and were processed and reconstructed in three dimensions with the FV10-ASW Viewer software (version 4.2, Olympus, Japan).

Quantification of images was carried out with Image-Pro Plus (Media Cybernetics, USA) according to previous reports and with some adjustment (Kusumbe et al., 2014; Schneider et al., 2017). Specifically, we lined out an area around the vessels with a range of 20 μm (Itkin et al., 2016) and quantified the fluorescence signals (parameter: area sum) within this area, which was regarded as the proteins/markers adjacent to type H or type L vessels (Figure S1B). For some indexes, after absolute quantification of the signals, we performed relative quantification by taking the numerical value of one group as the reference and calculating the relative values of other groups, shown as the fold changes.

Statistics

All data are represented as mean ± standard deviation (SD). Statistical significance was evaluated by two-tailed unpaired Student's t test for two-group comparison, or by one-way analysis of variation (ANOVA) followed by Newman-Keuls post-hoc tests for multiple comparisons in GraphPad Prism version 5.1 (GraphPad, USA). Values of $p < 0.05$ were considered as statistically significant.

Data and Code Availability

For details of the materials and methods used in this study, please refer to the Supplemental Information.

SUPPLEMENTAL INFORMATION

Supplemental Information can be found online at https://doi.org/10.1016/j.stemcr.2020.06.007.

AUTHOR CONTRIBUTIONS

J.C., M.L., and A.-Q.L. contributed equally to the experimental performing, data acquisition and analysis, and manuscript drafting. C.-X.Z., L.-H.B., and K.C. contributed to data analysis and

(E) *In vitro* tube formation by EC co-cultured with MSCs from Ctrl mice, EC co-cultured with DFM-pretreated MSCs, EC co-cultured with MSCs from Gli1$^+$ cell ablated mice, and EC co-cultured with DFM-pretreated MSCs from Gli1$^+$ cell ablated mice. Scale bars, 100 μm.
(F) Quantification of cumulative tube and branching lengths. n = 5 independent experiments.
(G) Diagram showing the synopsis of the findings.
**p < 0.01, ***p < 0.0001; NS, p > 0.05. Data are presented as mean ± SD.

interpretation. X.-L.X. and J.-T.G. contributed to animal experiments. M.B. contributed to flow cytometry analysis. T.Z. and B.-D.S. contributed to micro-CT analysis. D.-H.L., Y.J., and C.-H.H. contributed to the study conception and design, data interpretation, and manuscript revision.

ACKNOWLEDGMENTS

This work was supported by grants from The National Key Research and Development Program of China (2017YFA0104900), The National Natural Science Foundation of China (81930025 and 81570937), The Post-doctoral Innovative Talents Support Program of China (BX20190380 to B.-D.S.), The Young Elite Scientist Sponsorship Program by CAST of China (2019QNRC001 to B.-D.S.), The General Program of China Postdoctoral Science Foundation (2019M663986 to B.-D.S.), and The Youth Innovation Team of Shaanxi Universities.

Received: January 29, 2020
Revised: June 5, 2020
Accepted: June 8, 2020
Published: July 2, 2020

REFERENCES

Agarwal, S., Loder, S., Brownley, C., Cholok, D., Mangiavini, L., Li, J., Breuler, C., Sung, H.H., Li, S., Ranganathan, K., et al. (2016). Inhibition of Hif1alpha prevents both trauma-induced and genetic heterotopic ossification. Proc. Natl. Acad. Sci. U S A *113*, E338–E347.

Bijlsma, M.F., Groot, A.P., Oduro, J.P., Franken, R.J., Schoenmakers, S.H., Peppelenbosch, M.P., and Spek, C.A. (2009). Hypoxia induces a hedgehog response mediated by HIF-1alpha. J. Cell Mol. Med. *13*, 2053–2060.

Butler, J.M., Kobayashi, H., and Rafii, S. (2010). Instructive role of the vascular niche in promoting tumour growth and tissue repair by angiocrine factors. Nat. Rev. Cancer *10*, 138–146.

Caire, R., Roche, B., Picot, T., Aanei, C.M., He, Z., Campos, L., Thomas, M., Malaval, L., Vico, L., and Lafage-Proust, M.H. (2019). Parathyroid hormone remodels bone transitional vessels and the Leptin receptor-positive pericyte network in mice. J. Bone Mineral Res. *34*, 1487–1501.

Chen, N., Sui, B.D., Hu, C.H., Cao, J., Zheng, C.X., Hou, R., Yang, Z.K., Zhao, P., Chen, Q., Yang, Q.J., et al. (2016). microRNA-21 contributes to orthodontic tooth movement. J. Dental Res. *95*, 1425–1433.

Chen, Y., Whetstone, H.C., Lin, A.C., Nadesan, P., Wei, Q., Poon, R., and Alman, B.A. (2007). beta-Catenin signaling plays a disparate role in different phases of fracture repair: implications for therapy to improve bone healing. PLoS Med. *4*, e249.

Crisan, M., Yap, S., Casteilla, L., Chen, C.W., Corselli, M., Park, T.S., Andriolo, G., Sun, B., Zheng, B., Zhang, L., et al. (2008). A perivascular origin for mesenchymal stem cells in multiple human organs. Cell Stem Cell *3*, 301–313.

Ding, L., Saunders, T.L., Enikolopov, G., and Morrison, S.J. (2012). Endothelial and perivascular cells maintain haematopoietic stem cells. Nature *481*, 457–462.

Guimaraes-Camboa, N., Cattaneo, P., Sun, Y., Moore-Morris, T., Gu, Y., Dalton, N.D., Rockenstein, E., Masliah, E., Peterson, K.L., Stallcup, W.B., et al. (2017). Pericytes of multiple organs do not behave as mesenchymal stem cells in vivo. Cell Stem Cell *20*, 345–359 e345.

Hu, C.H., Sui, B.D., Du, F.Y., Shuai, Y., Zheng, C.X., Zhao, P., Yu, X.R., and Jin, Y. (2017). miR-21 deficiency inhibits osteoclast function and prevents bone loss in mice. Sci. Rep. *7*, 43191.

Huang, B., Wang, W., Li, Q., Wang, Z., Yan, B., Zhang, Z., Wang, L., Huang, M., Jia, C., Lu, J., et al. (2016). Osteoblasts secrete Cxcl9 to regulate angiogenesis in bone. Nat. Commun. *7*, 13885.

Itkin, T., Gur-Cohen, S., Spencer, J.A., Schajnovitz, A., Ramasamy, S.K., Kusumbe, A.P., Ledergor, G., Jung, Y., Milo, I., Poulos, M.G., et al. (2016). Distinct bone marrow blood vessels differentially regulate haematopoiesis. Nature *532*, 323–328.

Ivanova, A., Signore, M., Caro, N., Greene, N.D., Copp, A.J., and Martinez-Barbera, J.P. (2005). In vivo genetic ablation by Cre-mediated expression of diphtheria toxin fragment A. Genesis *43*, 129–135.

Jiang, J., and Hui, C.C. (2008). Hedgehog signaling in development and cancer. Dev. Cell *15*, 801–812.

Kalucka, J., de Rooij, L., Goveia, J., Rohlenova, K., Dumas, S.J., Meta, E., Conchinha, N.V., Taverna, F., Teuwen, L.A., Veys, K., et al. (2020). Single-cell transcriptome atlas of murine endothelial cells. Cell *180*, 764–779 e720.

Kasper, G., Dankert, N., Tuischer, J., Hoeft, M., Gaber, T., Glaeser, J.D., Zander, D., Tschirschmann, M., Thompson, M., Matziolis, G., et al. (2007). Mesenchymal stem cells regulate angiogenesis according to their mechanical environment. Stem Cells *25*, 903–910.

Kfoury, Y., and Scadden, D.T. (2015). Mesenchymal cell contributions to the stem cell niche. Cell Stem Cell *16*, 239–253.

Kramann, R., Goettsch, C., Wongboonsin, J., Iwata, H., Schneider, R.K., Kuppe, C., Kaesler, N., Chang-Panesso, M., Machado, F.G., Gratwohl, S., et al. (2016). Adventitial MSC-like cells are progenitors of vascular smooth muscle cells and drive vascular calcification in chronic kidney disease. Cell Stem Cell *19*, 628–642.

Kramann, R., Schneider, R.K., DiRocco, D.P., Machado, F., Fleig, S., Bondzie, P.A., Henderson, J.M., Ebert, B.L., and Humphreys, B.D. (2015). Perivascular Gli1+ progenitors are key contributors to injury-induced organ fibrosis. Cell Stem Cell *16*, 51–66.

Kusumbe, A.P., Ramasamy, S.K., and Adams, R.H. (2014). Coupling of angiogenesis and osteogenesis by a specific vessel subtype in bone. Nature *507*, 323–328.

Kusumbe, A.P., Ramasamy, S.K., Itkin, T., Mae, M.A., Langen, U.H., Betsholtz, C., Lapidot, T., and Adams, R.H. (2016). Age-dependent modulation of vascular niches for haematopoietic stem cells. Nature *532*, 380–384.

Kusumbe, A.P., Ramasamy, S.K., Starsichova, A., and Adams, R.H. (2015). Sample preparation for high-resolution 3D confocal imaging of mouse skeletal tissue. Nat. Protoc. *10*, 1904–1914.

Lei, J., Fan, L., Wei, G., Chen, X., Duan, W., Xu, Q., Sheng, W., Wang, K., and Li, X. (2015). Gli-1 is crucial for hypoxia-induced epithelial-mesenchymal transition and invasion of breast cancer. Tumour Biol. *36*, 3119–3126.

Lemos, D.R., and Duffield, J.S. (2018). Tissue-resident mesenchymal stromal cells: implications for tissue-specific antifibrotic therapies. Sci. Transl. Med. *10*, eaan5174.

Manieri, N.A., Mack, M.R., Himmelrich, M.D., Worthley, D.L., Hanson, E.M., Eckmann, L., Wang, T.C., and Stappenbeck, T.S. (2015). Mucosally transplanted mesenchymal stem cells stimulate intestinal healing by promoting angiogenesis. J. Clin. Invest. *125*, 3606–3618.

Mendez-Ferrer, S., Michurina, T.V., Ferraro, F., Mazloom, A.R., Macarthur, B.D., Lira, S.A., Scadden, D.T., Ma'ayan, A., Enikolopov, G.N., and Frenette, P.S. (2010). Mesenchymal and haematopoietic stem cells form a unique bone marrow niche. Nature *466*, 829–834.

Piard, C., Jeyaram, A., Liu, Y., Caccamese, J., Jay, S.M., Chen, Y., and Fisher, J. (2019). 3D printed HUVECs/MSCs cocultures impact cellular interactions and angiogenesis depending on cell-cell distance. Biomaterials *222*, 119423.

Ramasamy, S.K., Kusumbe, A.P., Wang, L., and Adams, R.H. (2014). Endothelial Notch activity promotes angiogenesis and osteogenesis in bone. Nature *507*, 376–380.

Red-Horse, K., Crawford, Y., Shojaei, F., and Ferrara, N. (2007). Endothelium-microenvironment interactions in the developing embryo and in the adult. Dev. Cell *12*, 181–194.

Schneider, R.K., Mullally, A., Dugourd, A., Peisker, F., Hoogenboezem, R., Van Strien, P.M.H., Bindels, E.M., Heckl, D., Busche, G., Fleck, D., et al. (2017). Gli1(+) mesenchymal stromal cells are a key driver of bone marrow fibrosis and an important cellular therapeutic target. Cell Stem Cell *20*, 785–800.e8.

Shang, F., Ming, L., Zhou, Z., Yu, Y., Sun, J., Ding, Y., and Jin, Y. (2014). The effect of licochalcone A on cell-aggregates ECM secretion and osteogenic differentiation during bone formation in metaphyseal defects in ovariectomized rats. Biomaterials *35*, 2789–2797.

Shi, S., and Gronthos, S. (2003). Perivascular niche of postnatal mesenchymal stem cells in human bone marrow and dental pulp. J. Bone Mineral Res. *18*, 696–704.

Shi, Y., He, G., Lee, W.C., McKenzie, J.A., Silva, M.J., and Long, F. (2017). Gli1 identifies osteogenic progenitors for bone formation and fracture repair. Nat. Commun. *8*, 2043.

Sivaraj, K.K., and Adams, R.H. (2016). Blood vessel formation and function in bone. Development *143*, 2706–2715.

Sugiyama, T., Kohara, H., Noda, M., and Nagasawa, T. (2006). Maintenance of the hematopoietic stem cell pool by CXCL12-CXCR4 chemokine signaling in bone marrow stromal cell niches. Immunity *25*, 977–988.

Sui, B., Hu, C., Zhang, X., Zhao, P., He, T., Zhou, C., Qiu, X., Chen, N., Zhao, X., and Jin, Y. (2016). Allogeneic mesenchymal stem cell therapy promotes osteoblastogenesis and prevents glucocorticoid-induced osteoporosis. Stem Cells Transl. Med. *5*, 1238–1246.

Sui, B.D., Hu, C.H., Liu, A.Q., Zheng, C.X., Xuan, K., and Jin, Y. (2019). Stem cell-based bone regeneration in diseased microenvironments: challenges and solutions. Biomaterials *196*, 18–30.

Wallner, C., Abraham, S., Wagner, J.M., Harati, K., Ismer, B., Kessler, L., Zollner, H., Lehnhardt, M., and Behr, B. (2016). Local application of isogenic adipose-derived stem cells restores bone healing capacity in a type 2 diabetes model. Stem Cells Transl. Med. *5*, 836–844.

Wang, Q.A., Song, A., Chen, W., Schwalie, P.C., Zhang, F., Vishvanath, L., Jiang, L., Ye, R., Shao, M., Tao, C., et al. (2018). Reversible de-differentiation of mature white adipocytes into preadipocyte-like precursors during lactation. Cell Metab. *28*, 282–288.e3.

Wang, Y., Wan, C., Deng, L., Liu, X., Cao, X., Gilbert, S.R., Bouxsein, M.L., Faugere, M.C., Guldberg, R.E., Gerstenfeld, L.C., et al. (2007). The hypoxia-inducible factor alpha pathway couples angiogenesis to osteogenesis during skeletal development. J. Clin. Invest. *117*, 1616–1626.

Xie, H., Cui, Z., Wang, L., Xia, Z., Hu, Y., Xian, L., Li, C., Xie, L., Crane, J., Wan, M., et al. (2014). PDGF-BB secreted by preosteoclasts induces angiogenesis during coupling with osteogenesis. Nat. Med. *20*, 1270–1278.

Xu, R., Yallowitz, A., Qin, A., Wu, Z., Shin, D.Y., Kim, J.M., Debnath, S., Ji, G., Bostrom, M.P., Yang, X., et al. (2018). Targeting skeletal endothelium to ameliorate bone loss. Nat. Med. *24*, 823–833.

Yang, M., Li, C.J., Sun, X., Guo, Q., Xiao, Y., Su, T., Tu, M.L., Peng, H., Lu, Q., Liu, Q., et al. (2017). MiR-497 approximately 195 cluster regulates angiogenesis during coupling with osteogenesis by maintaining endothelial Notch and HIF-1alpha activity. Nat. Commun. *8*, 16003.

Zhao, H., Feng, J., Ho, T.V., Grimes, W., Urata, M., and Chai, Y. (2015). The suture provides a niche for mesenchymal stem cells of craniofacial bones. Nat. Cell Biol. *17*, 386–396.

Zhao, H., Feng, J., Seidel, K., Shi, S., Klein, O., Sharpe, P., and Chai, Y. (2014). Secretion of shh by a neurovascular bundle niche supports mesenchymal stem cell homeostasis in the adult mouse incisor. Cell Stem Cell *14*, 160–173.

Zhao, P., Sui, B.D., Liu, N., Lv, Y.J., Zheng, C.X., Lu, Y.B., Huang, W.T., Zhou, C.H., Chen, J., Pang, D.L., et al. (2017). Anti-aging pharmacology in cutaneous wound healing: effects of metformin, resveratrol, and rapamycin by local application. Aging Cell *16*, 1083–1093.

Zheng, C.X., Sui, B.D., Qiu, X.Y., Hu, C.H., and Jin, Y. (2019). Mitochondrial regulation of stem cells in bone homeostasis. Trends Mol. Med. https://doi.org/10.1016/j.molmed.2019.04.008.

Zhou, B.O., Yue, R., Murphy, M.M., Peyer, J.G., and Morrison, S.J. (2014). Leptin-receptor-expressing mesenchymal stromal cells represent the main source of bone formed by adult bone marrow. Cell Stem Cell *15*, 154–168.

Stem Cell Reports, Volume *15*

Supplemental Information

Gli1^{+} Cells Couple with Type H Vessels and Are Required for Type H Vessel Formation

Ji Chen, Meng Li, An-Qi Liu, Chen-Xi Zheng, Li-Hui Bao, Kai Chen, Xiao-Lin Xu, Jiang-Tao Guan, Meng Bai, Tao Zhou, Bing-Dong Sui, De-Hua Li, Yan Jin, and Cheng-Hu Hu

Supplemental figures and legends

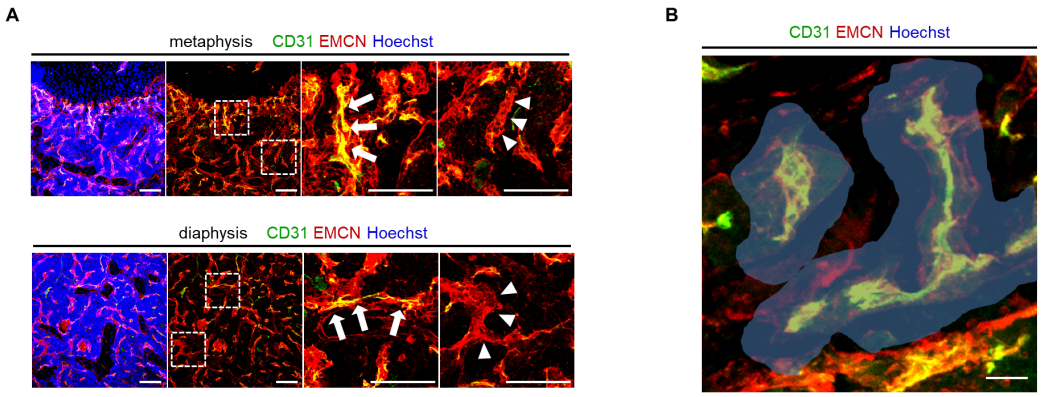

Figure S1. Properties of distinct types of blood vessels in bone and quantification method for adjacent cells. Related to Figure 1.

(A) Representative CD31 (green) and EMCN (red) co-immunostaining images indicating type H vessels (a, $CD31^{hi}EMCN^{hi}$, identified by arrows) and type L vessels (b, $CD31^{lo}EMCN^{lo}$, identified by arrowheads) in femoral metaphysis and diaphysis of mice, counterstained by Hoechst (blue). Boxed area is shown magnified to the right. Scale bars, 100 μm.

(B) Representative CD31 (green) and EMCN (red) co-immunostaining image indicating how the percentages of cells adjacent to specific blood vessels were scored. The fluorescence signals within the grey-masked areas which indicate the region of distance <20 μm around the blood vessels was quantified and regarded as the proteins/markers adjacent to type H or type L vessels. Scale bars, 20 μm.

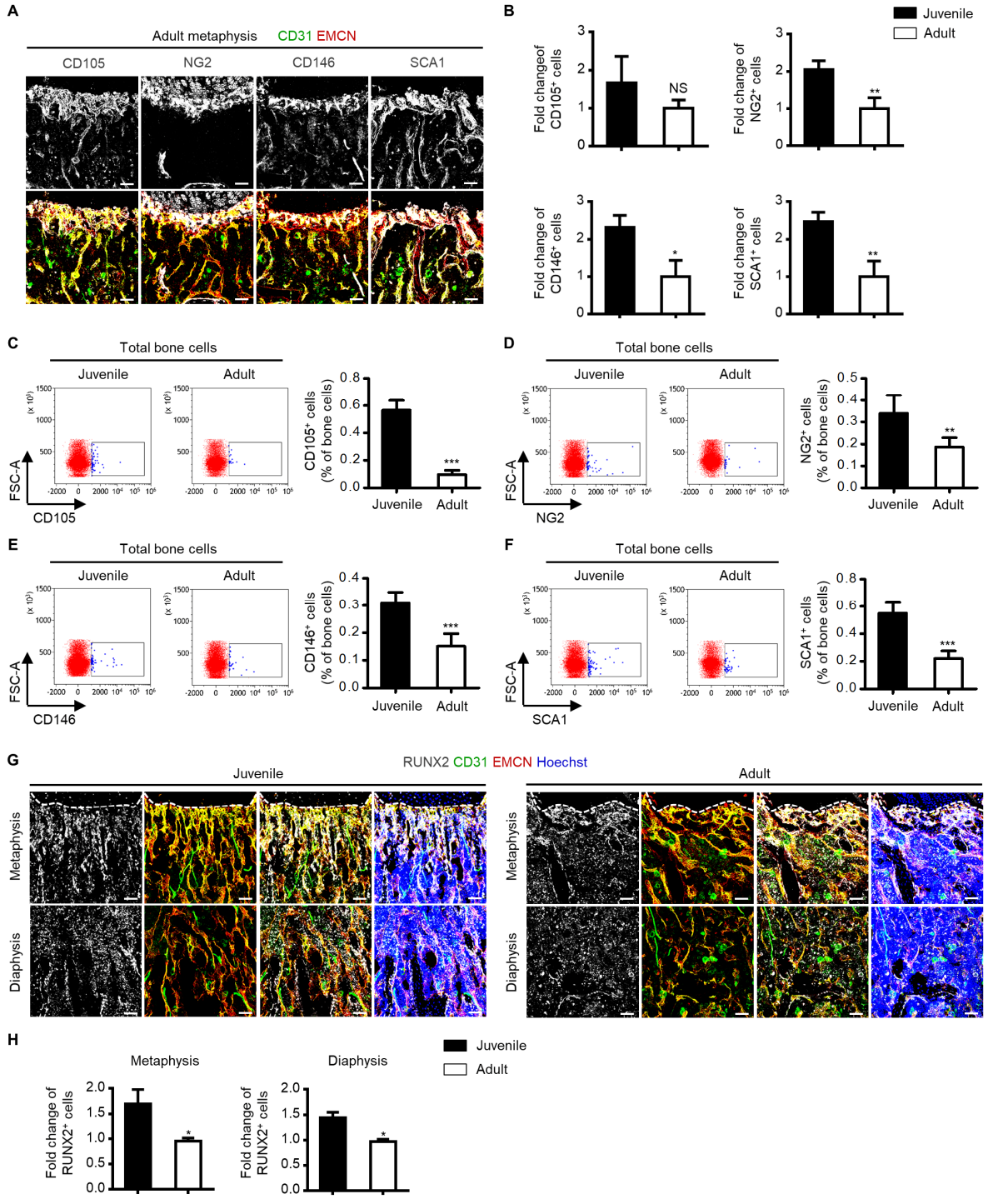

Figure S2. Spatial and Phenotypical Correlation of putative *in vivo* MSC markers and osteoprogenitor marker with Type H Vessels during Bone Growth. Related to Figure 2.

(A) CD31 (green), EMCN (red) and CD105, NG2, CD146 or SCA1 (white) co-immunostaining in femoral metaphysis of adult (8-week old) *Gli1-LacZ* mice. Scale bars, 100 μm.

(B) Quantification of fold changes of $CD105^+$, $NG2^+$, $CD146^+$ and $SCA1^+$ cells in metaphysis of juvenile (4-week old) and adult *Gli1-LacZ* mice. n=3~4 mice per group.

(C-F) Flow cytometric analysis of percentages of $CD105^+$ (C), $NG2^+$ (D), $CD146^+$ (E) and $SCA1^+$ (F) cells in total bone cells of juvenile and adult *Gli1-LacZ* mice. n=4~7 mice per group.

(G) RUNX2 (white), CD31 (green) and EMCN (red) co-immunostaining in femur of juvenile (4-week old) and adult (8-week old) *Gli1-LacZ* mice, counterstained by Hoechst (blue). Dotted lines outline margins of growth plates in metaphysis. Scale bars, 100 μm.

(H) Quantification of fold changes of $RUNX2^+$ cells in metaphysis and diaphysis of juvenile and adult *Gli1-LacZ* mice. n=3 mice per group.

*, $P<0.05$; **, $P<0.01$; ***, $P<0.0001$; NS, $P>0.05$. Data are presented as mean ± SD.

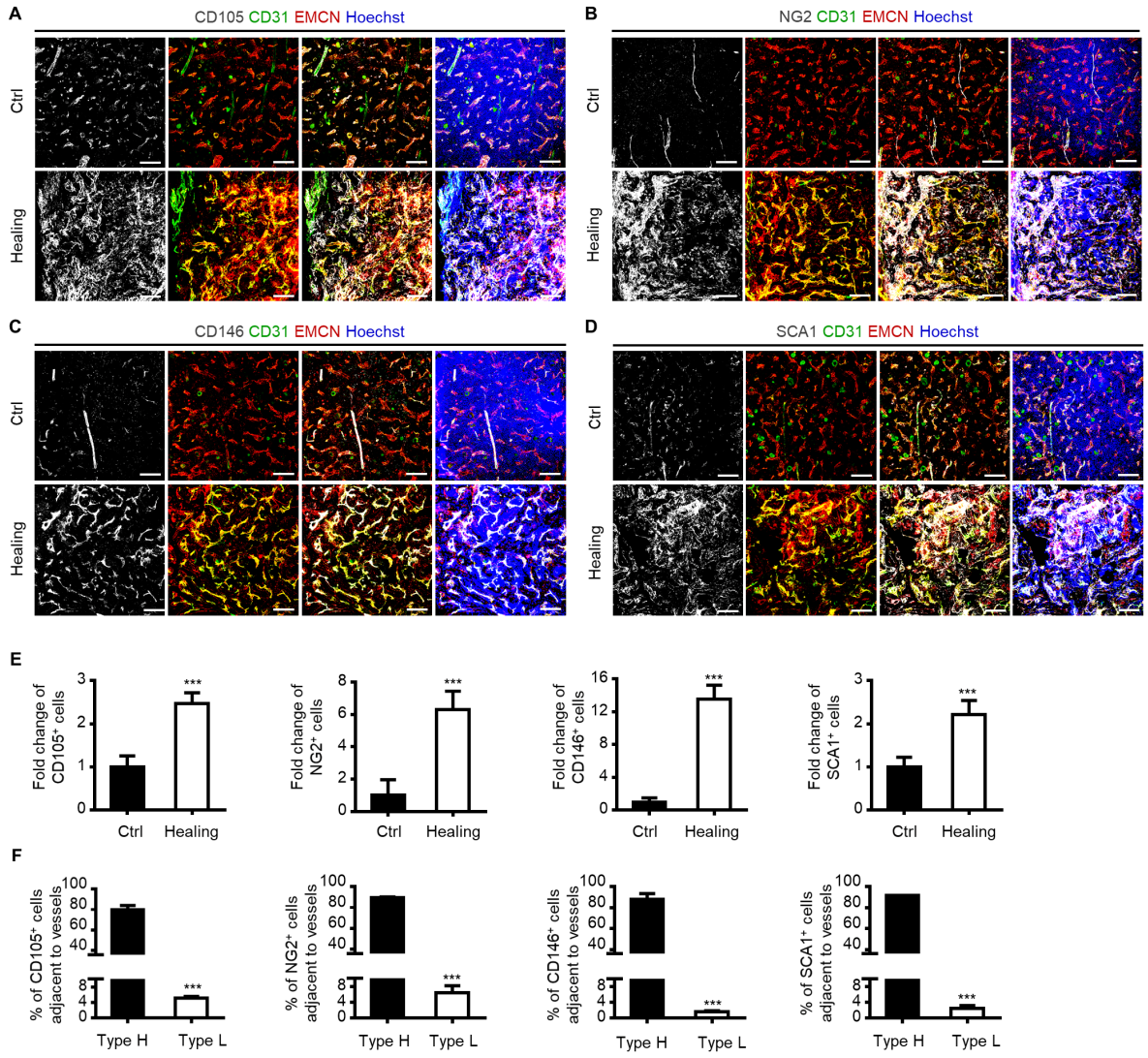

Figure S3. Correlation of MSCs with Type H Vessels in Bone Defect Healing. Related to Figure 3.

(A) CD105 (white), CD31 (green) and EMCN (red) co-immunostaining in femoral diaphysis from 10 week-old *Gli1-LacZ* mice without defects (Ctrl) or with healing defects at 2 weeks after femoral defect modeling, counterstained by Hoechst (blue). Scale bars, 100 μm.

(B) NG2 (white), CD31 (green) and EMCN (red) co-immunostaining in femoral diaphysis from 10 week-old *Gli1-LacZ* mice without defects (Ctrl) or with healing defects at 2 weeks after femoral defect modeling, counterstained by Hoechst (blue). Scale bars, 100 μm.

(C) CD146 (white), CD31 (green) and EMCN (red) co-immunostaining in femoral diaphysis from 10 week-old *Gli1-LacZ* mice without defects (Ctrl) or with healing defects at 2 weeks after femoral defect modeling, counterstained by Hoechst (blue). Scale bars, 100 μm.

(D) SCA1 (white), CD31 (green) and EMCN (red) co-immunostaining in femoral diaphysis from 10 week-old *Gli1-LacZ* mice without defects (Ctrl) or with healing defects at 2 weeks after femoral defect modeling, counterstained by Hoechst (blue). Scale bars, 100 μm.

(E) Quantification of fold changes of $CD105^+$, $NG2^+$, $CD146^+$ and $SCA1^+$ cells in Ctrl and healing area. n=3~6 mice per group.

(F) Quantification of percentages of $CD105^+$, $NG2^+$, $CD146^+$ and $SCA1^+$ cells adjacent to type H and type L

vessels in healing area. n=3 mice per group.

***, $P<0.0001$. Data are presented as mean ± SD.

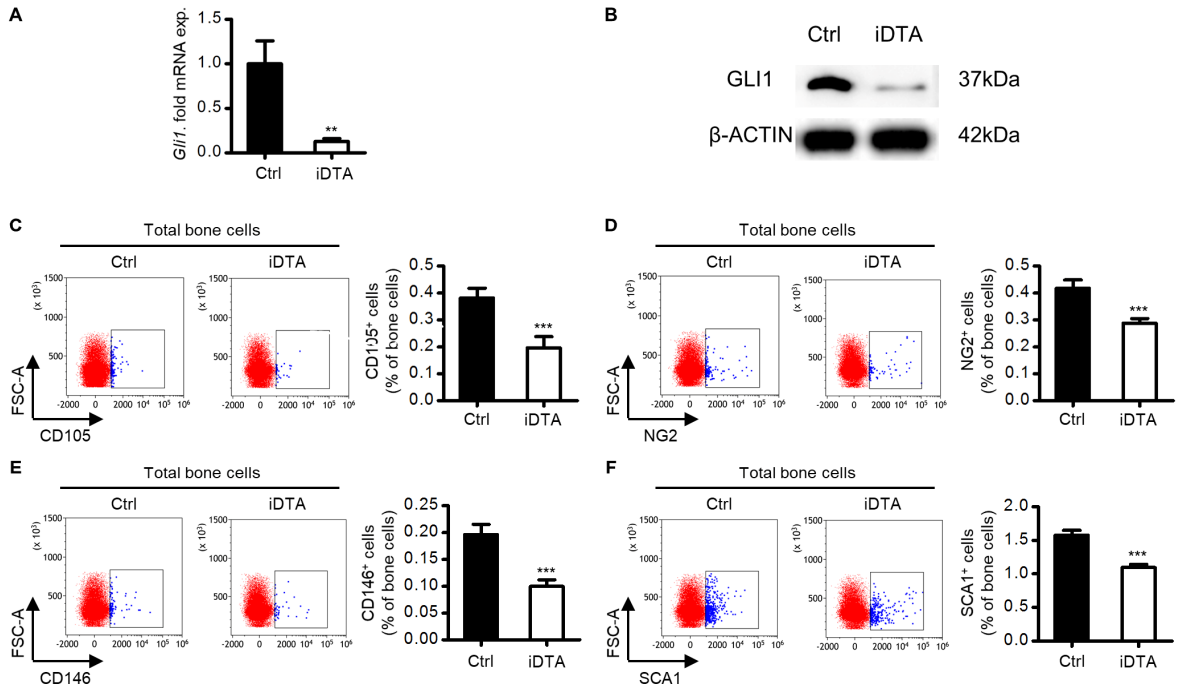

Figure S4. Genetic Ablation of Gli1$^+$ Cells in Bone. Related to Figure 4.

(A) qRT-PCR analysis of *Gli1* mRNA levels in bone tissues of Ctrl and Gli1$^+$ cell ablated mice, indicating ablation of Gli1$^+$ cells. n=3 mice per group.

(B) Western blotting analysis of GLI1 protein levels in bone tissues of Ctrl and Gli1$^+$ cell ablated mice, indicating ablation of Gli1$^+$ cells.

(C-F) Flow cytometric analysis of percentages of CD105$^+$ (A), NG2$^+$ (B), CD146$^+$ (C) and SCA1$^+$ (D) cells in total bone cells of Ctrl and Gli1$^+$ cell ablated mice. n=5 mice per group.

***, P<0.0001. Data are presented as mean ± SD.

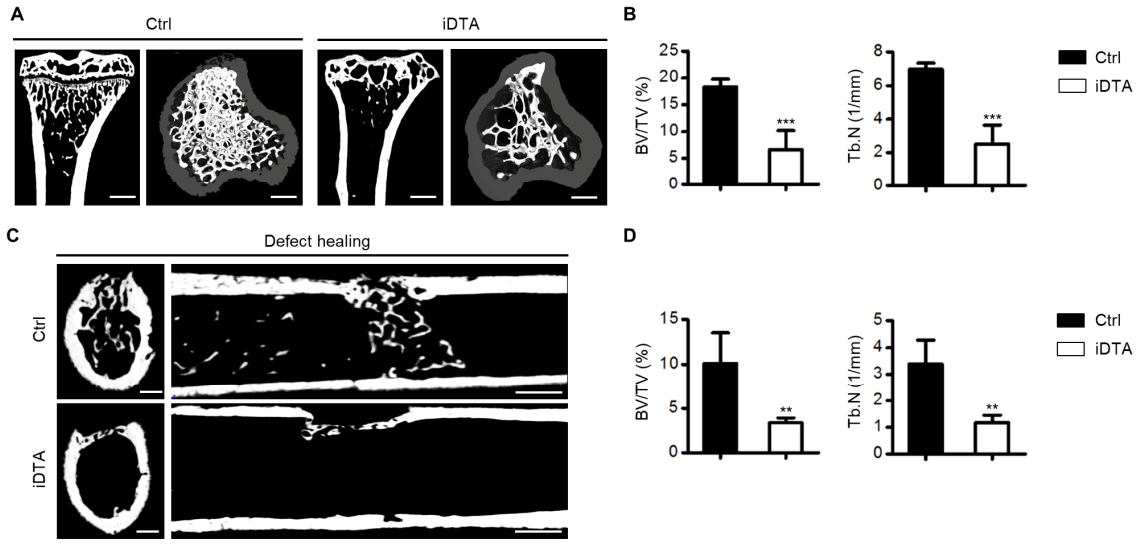

Figure S5. Genetic Ablation of Gli1$^+$ Cells Reduces Bone Mass during Growth and Healing. Related to Figure 4 and Figure 5.

(A) Micro-CT analysis of tibial bone mass in femur of Ctrl and Gli1$^+$ cell ablated mice. Images showing the median sagittal planes and 3-dimensional cross-sectional reconstruction. Scale bars, 500 μm.

(B) Quantification of bone volume and trabecular bone numbers. n=4~5 mice per group.

(C) Micro-CT analysis of defect healing in femur of Ctrl and Gli1$^+$ cell ablated mice. Images showing the median sagittal and coronal planes of healing defects. Scale bars, 200 μm (left) and 500 μm (right).

(D) Quantification of bone volume and trabecular bone numbers. n=4~6 mice per group.

**, P<0.01; ***, P<0.0001. Data are presented as mean ± SD.

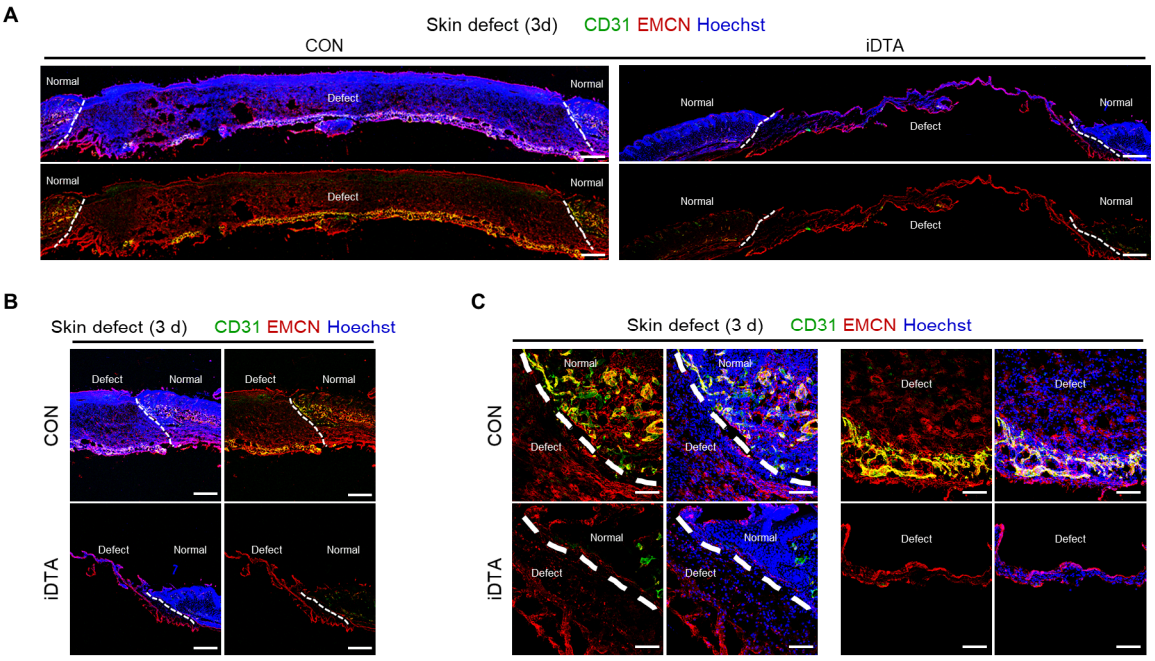

Figure S6. Genetic Ablation of Gli1$^+$ Cells Inhibits Type H Vessel Formation in Skin during Wound Healing. Related to Figure 5.

(A-C) CD31 (green) and EMCN (red) co-immunostaining in skin wound healing area of Ctrl and Gli1$^+$ cell ablated mice, counterstained by Hoechst (blue). Dotted lines outline the boundaries between defect and normal skin. Scale bars, 500 μm (A and B) and 100 μm (C).

Supplemental Experimental Procedures

Primary Cells and Cell Cultures

Total bone cells for flow cytometric analyses (Kusumbe et al., 2014; Schneider et al., 2017) were collected from tibiae and femora after removal of the adherent soft tissues. The hind limb bones were crushed in ice-cold PBS and were digested with collagenase (MP Biomedicals, USA) during incubation at 37°C for 60 min. Single cell suspensions were gathered after washing with PBS and filtration through 200-mesh cell strainers.

Mouse MSCs were isolated from hind limb bone marrow and cultured, as previously described (Lv et al., 2018; Sui et al., 2016; Sui et al., 2018). Briefly, primary mouse bone marrow cells were seeded into culture dishes, incubated overnight, and rinsed with PBS to remove the non-adherent cells. The adherent cells were cultured with alpha-minimum essential medium (α-MEM) supplemented with 20% fetal bovine serum (FBS), 2 mM L-glutamine, 100 U/ml penicillin and 100 g/ml streptomycin (all from Invitrogen, USA) at 37°C in a humidified atmosphere with 5% CO_2. After reaching confluence, MSCs were digested with 0.25% trypsin (MP Biomedicals, USA), passaged, and applied for assays.

Cell Lines

Human umbilical vein endothelial cell (HUVEC) line was purchased from ATCC and was maintained in Dulbecco's modified Eagle medium (DMEM) supplemented with 10% FBS, 2 mM L-glutamine, 100 U/ml penicillin and 100 g/ml streptomycin (all from Invitrogen, USA) at 37°C in a humidified atmosphere of 5% CO_2 (Jing et al., 2017).

Micro-CT Analysis

Freshly dissected hind limb bones were collected and were fixed in 4% PFA (Sigma-Aldrich, USA) solution overnight at 4°C, and were then prepared into 1-cm length specimens. The specimens were scanned at a resolution of 8 μm, a voltage of 80 kV and a current of 80 μA with a desktop micro-CT system (eXplore Locus SP, GE Healthcare, USA) (Sui et al., 2017; Zheng et al., 2018). After 3-dimensional image reconstruction, the region of interest (ROI) was selected in the tibial medial metaphysis or in the femoral defect area. Data were obtained with the VGStudio MAX software (Volume Graphics, Germany) using parameters of BV/TV and Tb.N, as recommended (Bouxsein et al., 2010).

Flow Cytometry

Total primary bone cells were analyzed. For analysis of $Gli1^+$ cells, total bone cells from *Gli1-CreER^{T2};mT/mG* mice were obtained and analyzed after induction of Cre activity by tamoxifen. For analysis of type H ECs, cells were subjected to immunostaining with EMCN antibody (PE-conjugated; sc-65495, Santa Cruz Biotechnology, USA; diluted 1:100) and CD31 antibody (Alexa Fluor 488-conjugated; FAB3628G, R&D Systems, USA; diluted 1:200) for 30 min at 4°C. For analysis of general MSCs, cells were immunostained with antibodies for CD105 (APC-conjugated; 120414, Biolegend, USA; diluted 1:200), NG2 (Alexa Fluor 647-conjugated; sc-53389, Santa Cruz Biotechnology, USA; diluted 1:200), CD146 (APC-conjugated; 134712, Biolegend, USA; diluted 1:100) and SCA1 (APC-conjugated; 108111, Biolegend, USA; diluted 1:200) for 30 min at 4°C. Cells were analyzed with a MoFlo XDP flow cytometer (Beckman Coulter, USA) equipped with the Kaluza software (Beckman Coulter, USA) for quantification (Kusumbe et al., 2014; Schneider et al., 2017).

Tube Formation Assay

As previously described (Xie et al., 2014), Matrigel (BD Biosciences, USA) was plated in 96-well culture plates and incubated at 37°C to polymerize for 45 min. HUVECs (2×10^4 cells/well) or HUVECs with MSCs (1×10^4 cells/well) were seeded onto polymerized Matrigel for 4 h. In indicated experiments, MSCs were pre-treated with

GANT61 (Cayman Chemical, USA), a specific Gli inhibitor (Schneider et al., 2017), DFM (MedChem Express, USA), a HIF-1α stabilizer and activator (Kusumbe et al., 2014), and PX-478 (MedChem Express, USA), a HIF-1α inhibitor (Agarwal et al., 2016), at 10 μM for 48 h. The tube formation of HUVECs was observed under a microscope and the cumulative tube and branching lengths were measured using the ImageJ software.

RNA isolation and qRT-PCR

Total RNA was extracted from bone marrow tissue using Trizol Reagent (Takara, Japan), and complementary DNA (cDNA) was generated using a PrimeScriptTM RT Reagent Kit (Takara, Japan). Then, qRT-PCR was performed with a SYBR Premix Ex Taq II Kit (Takara, Japan) by a Real-Time System (CFX96; Bio-Rad, USA). Quantification was performed by using *Gapdh* as the internal control. The primer sequences used are as follows: *Gli1*, forward 5'-CCAAGCCAACTTTATGTCAGGG-3', reverse 5'-AGCCCGCTTCTTTGTTAATTTGA-3'; *Gapdh*, forward 5'-TGTGTCCGTCGTGGATCTGA-3', reverse 5'-TTGCTGTTGAAGTCGCAGGAG-3'.

Western blotting

Western blotting was performed according to previously studies (Sui et al., 2017; Zhao et al., 2017). Briefly, proteins were extracted from bone marrow tissue and quantified using a BCA Protein Assay kit (TIANGEN, China). Equal amounts of protein samples were loaded onto SDS–PAGE gels, and transferred to polyvinylidene fluoride (PVDF) membranes (Millipore, USA) which were blocked with 5% BSA (Sigma-Aldrich, USA) in TBS for 2 h at room temperature. Then, the membranes were incubated overnight at 4℃ with the following primary antibodies: anti-GLI1 (TA309673, OriGene, USA) and anti-β-ACTIN (ab6276, Abcam, UK). The membranes were washed with TBS containing 0.1% Tween-20 and incubated with peroxidase-conjugated secondary antibodies (Boster, China) for 1 h at room temperature. The protein bands were visualized using an enhanced chemiluminescence kit (Amersham Biosciences, USA) and detected by a gel imaging system (4600; Tanon, China).

Supplemental References

Agarwal, S., Loder, S., Brownley, C., Cholok, D., Mangiavini, L., Li, J., Breuler, C., Sung, H.H., Li, S., Ranganathan, K., et al. (2016). Inhibition of Hif1alpha prevents both trauma-induced and genetic heterotopic ossification. Proceedings of the National Academy of Sciences of the United States of America *113*, E338-347.

Bouxsein, M.L., Boyd, S.K., Christiansen, B.A., Guldberg, R.E., Jepsen, K.J., and Muller, R. (2010). Guidelines for assessment of bone microstructure in rodents using micro-computed tomography. Journal of bone and mineral research : the official journal of the American Society for Bone and Mineral Research *25*, 1468-1486.

Jing, H., Liao, L., Su, X., Shuai, Y., Zhang, X., Deng, Z., and Jin, Y. (2017). Declining histone acetyltransferase GCN5 represses BMSC-mediated angiogenesis during osteoporosis. FASEB journal : official publication of the Federation of American Societies for Experimental Biology *31*, 4422-4433.

Kusumbe, A.P., Ramasamy, S.K., and Adams, R.H. (2014). Coupling of angiogenesis and osteogenesis by a specific vessel subtype in bone. Nature *507*, 323-328.

Lv, Y.J., Yang, Y., Sui, B.D., Hu, C.H., Zhao, P., Liao, L., Chen, J., Zhang, L.Q., Yang, T.T., Zhang, S.F., et al. (2018). Resveratrol counteracts bone loss via mitofilin-mediated osteogenic improvement of mesenchymal stem cells in senescence-accelerated mice. Theranostics *8*, 2387-2406.

Schneider, R.K., Mullally, A., Dugourd, A., Peisker, F., Hoogenboezem, R., Van Strien, P.M.H., Bindels, E.M., Heckl, D., Busche, G., Fleck, D., et al. (2017). Gli1(+) Mesenchymal Stromal Cells Are a Key Driver of Bone Marrow Fibrosis and an Important Cellular Therapeutic Target. Cell stem cell *20*, 785-800 e788.

Sui, B., Hu, C., Liao, L., Chen, Y., Zhang, X., Fu, X., Zheng, C., Li, M., Wu, L., Zhao, X., et al. (2016). Mesenchymal progenitors in osteopenias of diverse pathologies: differential characteristics in the common shift from osteoblastogenesis to adipogenesis. Scientific reports *6*, 30186.

Sui, B.D., Chen, J., Zhang, X.Y., He, T., Zhao, P., Zheng, C.X., Li, M., Hu, C.H., and Jin, Y. (2018). Gender-independent efficacy of mesenchymal stem cell therapy in sex hormone-deficient bone loss via immunosuppression and resident stem cell recovery. Experimental & molecular medicine *50*, 166.

Sui, B.D., Hu, C.H., Zheng, C.X., Shuai, Y., He, X.N., Gao, P.P., Zhao, P., Li, M., Zhang, X.Y., He, T., et al. (2017). Recipient Glycemic Micro-environments Govern Therapeutic Effects of Mesenchymal Stem Cell Infusion on Osteopenia. Theranostics *7*, 1225-1244.

Xie, H., Cui, Z., Wang, L., Xia, Z., Hu, Y., Xian, L., Li, C., Xie, L., Crane, J., Wan, M., et al. (2014). PDGF-BB secreted by preosteoclasts induces angiogenesis during coupling with osteogenesis. Nature medicine *20*, 1270-1278.

Zhao, P., Sui, B.D., Liu, N., Lv, Y.J., Zheng, C.X., Lu, Y.B., Huang, W.T., Zhou, C.H., Chen, J., Pang, D.L., et al. (2017). Anti-aging pharmacology in cutaneous wound healing: effects of metformin, resveratrol, and rapamycin by local application. Aging cell *16*, 1083-1093.

Zheng, C.X., Sui, B.D., Liu, N., Hu, C.H., He, T., Zhang, X.Y., Zhao, P., Chen, J., Xuan, K., and Jin, Y. (2018). Adipose mesenchymal stem cells from osteoporotic donors preserve functionality and modulate systemic inflammatory microenvironment in osteoporotic cytotherapy. Scientific reports *8*, 5215.